THE ASTROPHYSICAL JOURNAL, 419:707–724, 1993 December 20

STRUCTURE OF DENSE CORES IN M17 SW. I. A MULTITRANSITION CS AND $C^{34}S$ STUDY

YANGSHENG WANG,[1] DANIEL T. JAFFE,[1] NEAL J. EVANS II,[1] MASAHIKO HAYASHI,[2]
KEN'ICHI TATEMATSU,[1] AND SHUDONG ZHOU[3]
Received 1993 March 18; accepted 1993 July 1

ABSTRACT

We present results of a multitransition CS and $C^{34}S$ study of the M17 SW molecular cloud core. Fully sampled maps were obtained in the CS $J = 1 \rightarrow 0$, $2 \rightarrow 1$, and $7 \rightarrow 6$ lines and the $C^{34}S$ $J = 2 \rightarrow 1$ line with 18″–36″ resolution. Velocity channel maps reveal the clumpy emission from the dense gas on scales of $\sim$0.2 pc (20″). The overall agreement in the cloud morphology among maps of different CS and $C^{34}S$ transitions suggests that all CS and $C^{34}S$ lines originate in the same dense gas. Excitation and opacity effects probably cause the modest differences between the maps.

We carried out a detailed excitation analysis of the multitransition data. The $J = 2 \rightarrow 1$ and $J = 7 \rightarrow 6$ transitions of CS, analyzed with a large velocity gradient (LVG) radiative transfer model, produced 250 pixel maps of the volume density and the CS column density over an area of about 1.8 pc × 2.4 pc. Peaks in the CS and the $C^{34}S$ line temperature maps are maxima in column density, but not in density. The density maps shows a fairly uniform, high density ($n \sim 10^{5.7}$ cm^{-3}) throughout the cloud core. An independent estimate of the gas densities from analysis of the $C^{34}S$ observations confirms the CS results. Along with other evidence, these results imply a clumpy cloud model in which the CS emission arises from structures smaller than our beam.

We compared the observed CS maps with a specific clumpy cloud model with 179 clumps decomposed from the $C^{18}O$ $J = 2 \rightarrow 1$ maps (Stutzki & Güsten 1990). Model channel maps of CS were synthesized based on the clump parameters listed in Stutzki & Güsten (1990) and were compared with the observed maps. The gas densities used in the models were derived from the clump column densities (based on the $C^{18}O$ $J = 2 \rightarrow 1$ emission) and sizes. Most of the dominant clumps had densities near 10^5 cm^{-3}. The resulting synthesized map does not reproduce the observed CS $J = 7 \rightarrow 6$ emission along the eastern ridge of the core. By assuming a constant gas density for all clumps, we were able to synthesize CS channel maps which reproduce the observed cloud morphology and the line intensities reasonably well. A mean clump density in the models of about 5×10^5 cm^{-3} (about 5 times higher than the density derived from $C^{18}O$) matches the observed CS line ratios and a CS/H_2 abundance ratio of about 4×10^{-9} fits the observed line intensities of the $J = 1 \rightarrow 0$, $2 \rightarrow 1$, and $7 \rightarrow 6$ transitions of CS. The discrepancy between densities derived from $C^{18}O$ and CS can be resolved if the clumps have internal density structure. Either smooth density gradients in clumps with sizes just below our angular resolution or a continuation of high-contrast clumping to still smaller scales could account for the difference. While we cannot rule out either of these pictures, it is noteworthy that the scale of the $C^{18}O$ observations ($\sim$0.15 pc) is the largest for which the density discrepancy can be resolved with smooth density gradients in unresolved clumps.

Subject headings: H II regions — ISM: individual (M17) — ISM: molecules — ISM: structure — radio lines: ISM

1. INTRODUCTION

Mapping the gas density in star-forming molecular clouds provides quantitative information about their internal structure. The dense cores ($n \gtrsim 10^4$ cm^{-3}) inferred from intensity peaks in molecular line maps of high density tracers (e.g., NH_3, CS, and H_2CO) are sites of enhanced star formation (see, for example, Myers 1987; Lada 1992). However, molecular line maps should be interpreted with excitation models in order to understand the physical nature of dense cores. The multitransition technique, using several transitions with high critical densities from molecules such as CS, H_2CO, and HCN, is an effective way to determine the local gas density in star-forming regions (Snell et al. 1984; Mundy et al. 1987; Evans et al. 1987).

CS has a number of advantages as a density tracer. Many CS rotational transitions can be observed at millimeter and submillimeter wavelengths. In addition, ^{34}S is only $\sim$20 times less abundant than ^{32}S, making $C^{34}S$ an easily detectable, yet usually optically thin, species. Observing $C^{34}S$ provides constraints on the effect of photon trapping and independent estimates of the density (Mundy et al. 1986).

Previous CS and $C^{34}S$ multitransition studies employed telescope beams of $\sim$1′ to 2′ and analyzed the data with the large velocity gradient (LVG) radiative transfer model (Snell et al. 1984; Mundy et al. 1986). These studies revealed extended dense gas ($n \sim 10^{5-6}$ cm^{-3}) but found very little systematic density variation across individual sources, in contrast to the factor of $\gtrsim$10 variations in the column density of the tracer molecules. The results could be understood if these regions contain numerous unresolved, dense (10^{5-6} cm^{-3}) clumps. Variations in the clump filling factor with position would then produce the appearance of variations in column density.

Can improved spatial resolution reveal the clumps inferred in the multitransition studies? High-resolution ($\sim$10″) maps of the regions studied with multitransition methods show many compact emission peaks (Mezger et al. 1988; Moore et al.

[1] Astronomy Department, The University of Texas, Austin, TX 78712.
[2] Astronomy Department, The University of Tokyo, Bunkyo-ku, Tokyo 113, Japan.
[3] Astronomy Department, The University of Illinois, Urbana, IL 61801.

1989; Schulz et al. 1991; Welch et al. 1987). Observers usually assume that these emission peaks are clumps of gas with enhanced density. A clump deconvolution procedure applied to a $C^{18}O$ $J = 2 \rightarrow 1$ map (13″ resolution) of M17 SW (Stutzki & Güsten 1990) produced 179 clumps with sizes down to 0.05 pc.

Do the emission peaks seen in molecular line maps with a resolution of about 0.1 pc represent real density enhancements within molecular clouds or are they regions of enhanced filling factor of still smaller clumps? High-resolution observations of a single molecular line cannot answer this question. Observations of multiple transitions of a single molecule and models of molecular excitation and radiative transport are necessary to determine the density at the peaks seen in the molecular line maps. The goal of this work is to determine if the emission peaks with diameters of 0.14–0.5 pc in M17 SW represent actual clumps or merly enhancements in the filling factor of still unresolved structure, as was found on a scale of $\gtrsim 0.7$ pc (Snell et al. 1984). The answer to this question has important consequences for studies of the relationship between cloud structure and fragmentation in massive cores and the formation and properties of stellar clusters or associations.

The M17 SW molecular cloud core lies southwest of the optical H II region, M17 (NGC 6618). The cloud core is the brightest peak in the CO emission from a much larger, filamentary ($\sim$140 pc long) molecular cloud complex (Elmegreen, Lada, & Dickinson 1979), a relatively nearby example of the clouds which dominate star formation in the Galaxy (Jaffe & Fazio 1982). The infrared luminosity of M17 is about 6×10^6 $L_\odot$ (Harper et al. 1976), $\sim$50–100 times that of the Orion A region. M17 SW has been studied extensively in various molecular and atomic lines (Lada 1976; Elmegreen & Lada 1976; Thronson & Lada 1983; Güsten & Fiebig 1988; Schulz & Krügel 1987; Rainey et al. 1987; Stutzki et al. 1988; Stutzki & Güsten 1990; Meixner et al. 1992; Greaves, White, & Williams 1992; Hobson 1992). High-resolution radio continuum maps (Felli et al. 1984) confirmed early indications that the H II/H_2 interface region is viewed almost edge-on (Gatley et al. 1979; Wilson et al. 1979). Within M17 SW, an infrared point source (Kleinmann & Wright 1970), an ultracompact H II region (Felli, Churchwell, & Masse 1984), and several H_2O masers (Downes et al. 1980; Jaffe, Güsten, & Downes 1981) provide evidence of ongoing star formation (see also Lada et al. 1991). Estimates for the distance to M17 range from 1.3 kpc to 2.2 kpc (Ogura & Ishida 1976; Crampton, Georgelin, & Georgelin 1978; Downes et al. 1980). We adopted a distance of 2.2 kpc, derived from the multicolor study of the star cluster associated with the optical H II region (Chini, Elsässer, & Neckel 1980).

We have carried out a multitransition study of the M17 SW core with resolutions of 18″–36″ in both CS and $C^{34}S$. Almost all of the data were taken with very similar beamsizes (18″–20″). The main objective was to obtain a map of the volume density over a large area, with spatial resolution comparable to that used by Stutzki & Güsten (1990). We present the observational results in § 3. A detailed LVG excitation analysis of the multitransition CS and $C^{34}S$ data is described in § 4. In § 5, the multitransition CS observations are compared with the clump model proposed by Stutzki & Güsten (1990). We summarize the results in § 6.

2. OBSERVATIONS

Our data set includes fully sampled maps of M17 SW in the CS $J = 7 \rightarrow 6$, CS $J = 2 \rightarrow 1$, CS $J = 1 \rightarrow 0$, and $C^{34}S$ $J = 2 \rightarrow 1$ lines, and more limited observations of the $C^{34}S$ $J = 7 \rightarrow 6$ and CS $J = 5 \rightarrow 4$ transitions. We used two different telescopes in order to obtain comparable beam sizes for different lines. Our analysis also uses the $C^{34}S$ $J = 3 \rightarrow 2$ observations of Stutzki & Güsten (1990), who kindly provided us with their data. The observing parameters are summarized in Table 1.

TABLE 1

OBSERVING PARAMETERS

Line	Frequency (GHz)	Telescope	θ_b	ΔV (km s^{-1})	η_{mb}
CS $J = 1 \rightarrow 0$	48.9910	...	36″	0.13	0.67[a]
CS $J = 2 \rightarrow 1$	97.9810	NRO	18	0.13 0.83	0.50[b]
$C^{34}S$ $J = 2 \rightarrow 1$	96.4130	...	18	0.13 0.83	0.48[b]
CS $J = 5 \rightarrow 4$	244.9356	...	30	1.6	0.72[c]
CS $J = 7 \rightarrow 6$	342.8830	CSO	20	1.0	0.60[c]
$C^{34}S$ $J = 7 \rightarrow 6$	337.3966	...		1.0	0.60[c]

[a] Nobeyama Radio Observatory Newsletter 1991.
[b] Our measurements.
[c] Caltech Submillimeter Observatory Memo 1989.

We observed the CS $J = 7 \rightarrow 6$ line and the $C^{34}S$ $J = 7 \rightarrow 6$ line, using the CSO[4] 10.4 m telescope in 1989 June and 1990 July and August. The 345 GHz SIS receiver operated in double-sideband mode with the centers of the two sidebands separated by 2.8 GHz. We assumed the sideband gain ratio to be unity in the calibration. The backend was an acousto-optic spectrometer (AOS) with 1024 channels over a bandwidth of 500 MHz. Pointing checks were made regularly during each night by observing the CO $J = 3 \rightarrow 2$ emission from CRL 618, CRL 2688, or *o* Ceti. The pointing was repeatable to $\lesssim 4''$. For observations of M17 SW, the telescope switched between the source and a fixed off position ($\alpha[1950.0] = 18^h18^m09^s$, $\delta[1950.0] = -16°09'55''$), which is free of CO $J = 1 \rightarrow 0$ emission (Elmegreen et al. 1979; Thronson & Lada 1983). We mapped a $3' \times 4'$ region with 272 positions on a 12″ grid in the CS $J = 7 \rightarrow 6$ line with typical integration times of 60 s on and 60 s off the source, resulting in an rms noise of $\lesssim 0.2$ K. For the $C^{34}S$ $J = 7 \rightarrow 6$ spectra along a declination cut, a right ascension cut, and at other selected locations, typical integration time was 10 minutes on source, and the rms noise was ~ 0.06 K. In addition, we obtained about 20 CS $J = 5 \rightarrow 4$ (244.9356 GHz) spectra toward the local intensity peaks in 1991 July and August at the CSO.

The CS $J = 2 \rightarrow 1$, $C^{34}S$ $J = 2 \rightarrow 1$, and CS $J = 1 \rightarrow 0$ lines were mapped in 1990 February and 1991 February with the 45 m telescope of the Nobeyama Radio Observatory (NRO). The CS $J = 2 \rightarrow 1$ and $C^{34}S$ $J = 2 \rightarrow 1$ maps were obtained simultaneously with a Schottky receiver and an SIS receiver. For each line, we used two AOS backends, one with a 250 MHz bandwidth and the other with a 40 MHz bandwidth. We also repeated the $C^{34}S$ $J = 2 \rightarrow 1$ map while obtaining a CS $J = 1 \rightarrow 0$ map using an SIS receiver. All three receivers were equipped with cooled single-sideband filters. We checked the pointing regularly by observing VX Sgr in the SiO $v = 1$, $J = 1 \rightarrow 0$ maser line (43.122 GHz) and the $v = 2$, $J = 1 \rightarrow 0$ maser line (42.820 GHz). The pointing was accurate to $\pm 5''$

[4] The CSO is operated by the California Institute of Technology under funding from the National Science Foundation, contract AST 90-15755.

rms. The observations were also made by position switching, using the same off position as used for the $J = 7 \rightarrow 6$ observations. All the observations were carried out on the same 12″ grid described above, but over a larger area of 4′ × 5′ with 433 data points. Typical on-source integration times were 1 minute for the CS $J = 2 \rightarrow 1$ and $J = 1 \rightarrow 0$ lines and 2 minutes for the $C^{34}S$ $J = 2 \rightarrow 1$ line (5 minutes at selected positions). The rms noise was about 0.2 K for the $C^{34}S$ $J = 2 \rightarrow 1$ and the CS $J = 1 \rightarrow 0$ spectra and about 0.4 K for the CS $J = 2 \rightarrow 1$ spectra with the 250 MHz AOS.

The standard chopper-wheel calibration procedure (Penzias & Burrus 1973) was used for both the CSO and the NRO observations. The resulting antenna temperatures (T_A^*) are corrected for the atmospheric opacity and the antenna rear spillover and scattering. We obtained main-beam radiation temperatures, T_{mb}, by dividing T_A^* by the main-beam efficiencies (η_{mb}) listed in Table 1. Technically, η_{mb} is the fraction of the power not terminated at ambient temperature which falls within the first nulls of the antenna power pattern; this is η_B/η_{rss}, where η_B is the beam efficiency as defined by Kraus (1986) and η_{rss} is the rearward spillover and scattering efficiency defined by Kutner & Ulich (1981). For a source which uniformly fills the main diffraction beam, T_{mb} is equivalent to T_R in the notation of Kutner & Ulich (1981) if there is no significant coupling of sidelobes to the source. The existence of sidelobes means that T_{mb} may be larger than T_R for sources larger than the main beam. During our NRO run in 1991 February, the calibration was checked by observing Jupiter in spectral line mode at the frequencies of the $J = 2 \rightarrow 1$ lines of CS and $C^{34}S$. Assuming a brightness temperature of 160 K for Jupiter, the main-beam efficiency was 0.48 for the SIS receiver and 0.50 for the Schottky receiver. Our measurements are con-

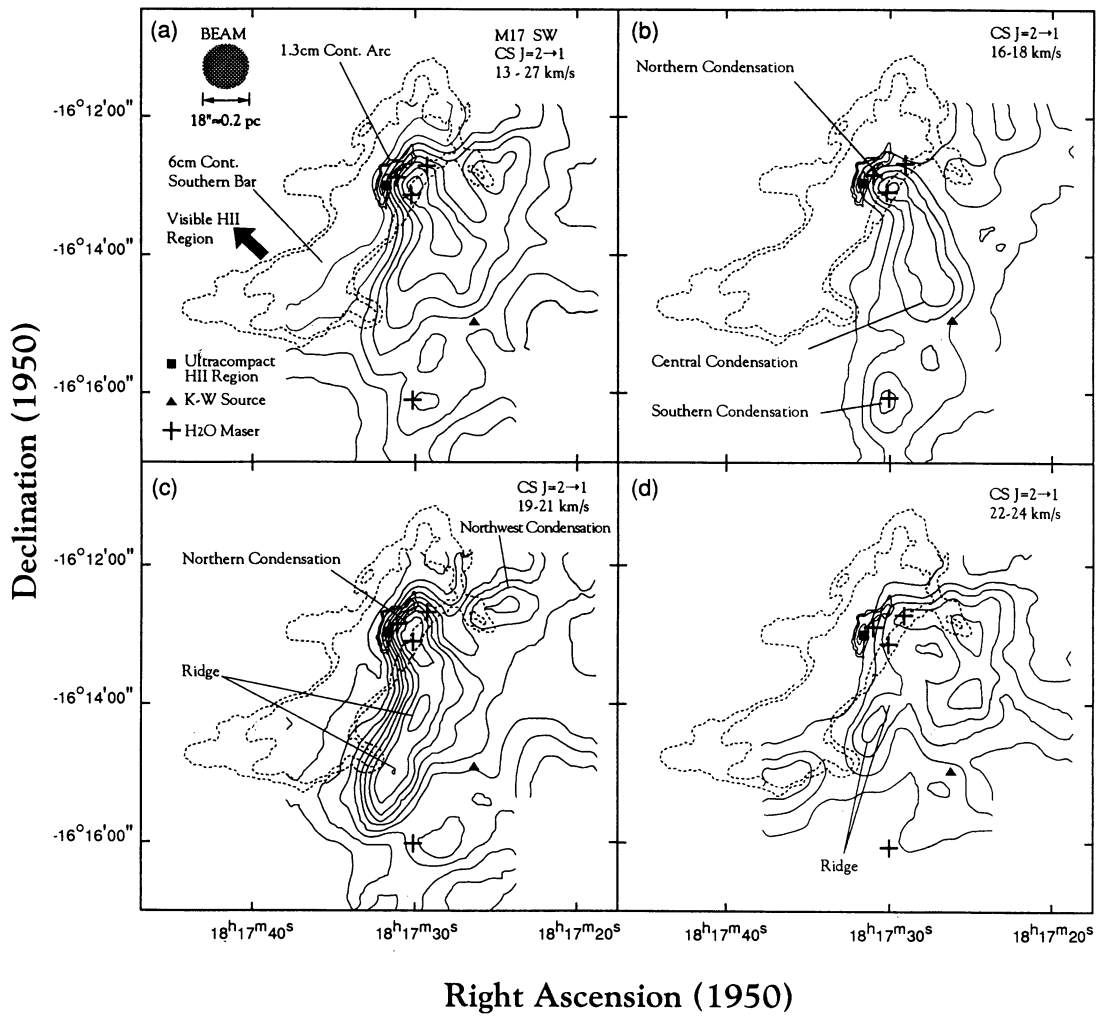

FIG. 1.—(*a*) Integrated intensity map of the CS $J = 2 \rightarrow 1$ line (*solid lines*), superposed on the 6 cm radio continuum emission (*thin, dashed lines*) (Felli et al. 1984) and the 1.3 cm continuum arc (*thin, solid lines*) (Felli et al. 1984). The positions of H_2O masers (*crosses*; Jaffe et al. 1981), the ultracompact H II region (*filled square*; Felli et al. 1984), and a near-IR source (*filled triangle*; Kleinmann & Wright 1973) are indicated. (*b*) CS $J = 2 \rightarrow 1$ intensity integrated from 16 to 18 km s^{-1} superposed on the 6 cm and the 1.3 cm continuum maps. (*c*) CS $J = 2 \rightarrow 1$ intensity integrated from 19 to 21 km s^{-1} superposed on the radio continuum maps. (*d*) CS $J = 2 \rightarrow 1$ intensity integrated from 22 to 24 km s^{-1} superposed on the radio continuum maps. The main features discussed in § 3 are identified. The lowest contour and the contour step for the CS $J = 2 \rightarrow 1$ integrated intensity map (Fig. 1*a*) is 7.5 K km s^{-1}; the lowest contours and the contour steps for the CS $J = 2 \rightarrow 1$ channel maps (Figs. 1*b*, 1*c*, and 1*d*) are 2 K km s^{-1}.

sistent with previous NRO measurements to within ±10% (T. Umemoto, private communication). The beam sizes at NRO (FWHM) were measured by observing 3C 84.

3. RESULTS

3.1. CS *Mapping Results*

Figure 1 shows the CS $J = 2 \rightarrow 1$ emission toward M17 SW and its relation to other features of the region. The cloud core lies just west of the 6 cm continuum emission rim (Felli et al.1984). Substructures with sizes of ~30″–120″ exist throughout the mapped area in the CS integrated intensity maps (Figs. 2*a* and 2*b*), as well as in the velocity channel maps of the CS $J = 7 \rightarrow 6$ (Fig. 3) and $J = 2 \rightarrow 1$ lines (Fig. 4). Several features apparent in the 13″ resolution $C^{18}O$ $J = 2 \rightarrow 1$ map (Stutzki & Güsten 1990) also appear in our CS maps. A prominent maximum (the "northern condensation," following Stutzki & Güsten 1990), just west of the ultracompact H II region and the associated 1.3 cm continuum arc, and an elongated emission feature along the H II/H_2 interface (the "ridge") dominate the CS emission of M17 SW (Figs. 1*b* and 1*c*). The northern condensation is the major center of activity along the H_2/H II interface and it is associated with the 1.3 cm continuum arc, the ultracompact H II region, and three H_2O masers (Fig. 1*b*). A local minimum (hole) west of the northern condensation is seen in the CS $J = 2 \rightarrow 1$ and $C^{34}S$ $J = 2 \rightarrow 1$ maps (Figs. 2*b* and 2*c*) but is not as well-defined in the maps of the CS $J = 1 \rightarrow 0$ and $J = 7 \rightarrow 6$ lines. The previous CS $J = 7 \rightarrow 6$ map of Snell et al. (1986) is consistent with our map (Fig. 2*a*). Allowing for the somewhat larger extent of the $J = 2 \rightarrow 1$ map, the overall size of the CS $J = 7 \rightarrow 6$ emission is comparable to that of the CS $J = 2 \rightarrow 1$ emission, implying that the gas density does not differ appreciably between the center and the edges of the source.

All of the CS features are better seen in the velocity channel maps (Figs. 3 and 4), where the emission from the northern condensation appears in almost all velocity channels but the ridge at the interface only appears clearly at $V_{LSR} \sim 19$–21 km s^{-1} (see also Fig. 1*c*). An extended (~1′) maximum (the "central condensation") appears in the middle of the mapped region at 16–19 km s^{-1} (see also Fig. 1*b*). This feature coincides with the 40″ resolution NH_3 (2, 2) emission peak (Güsten &

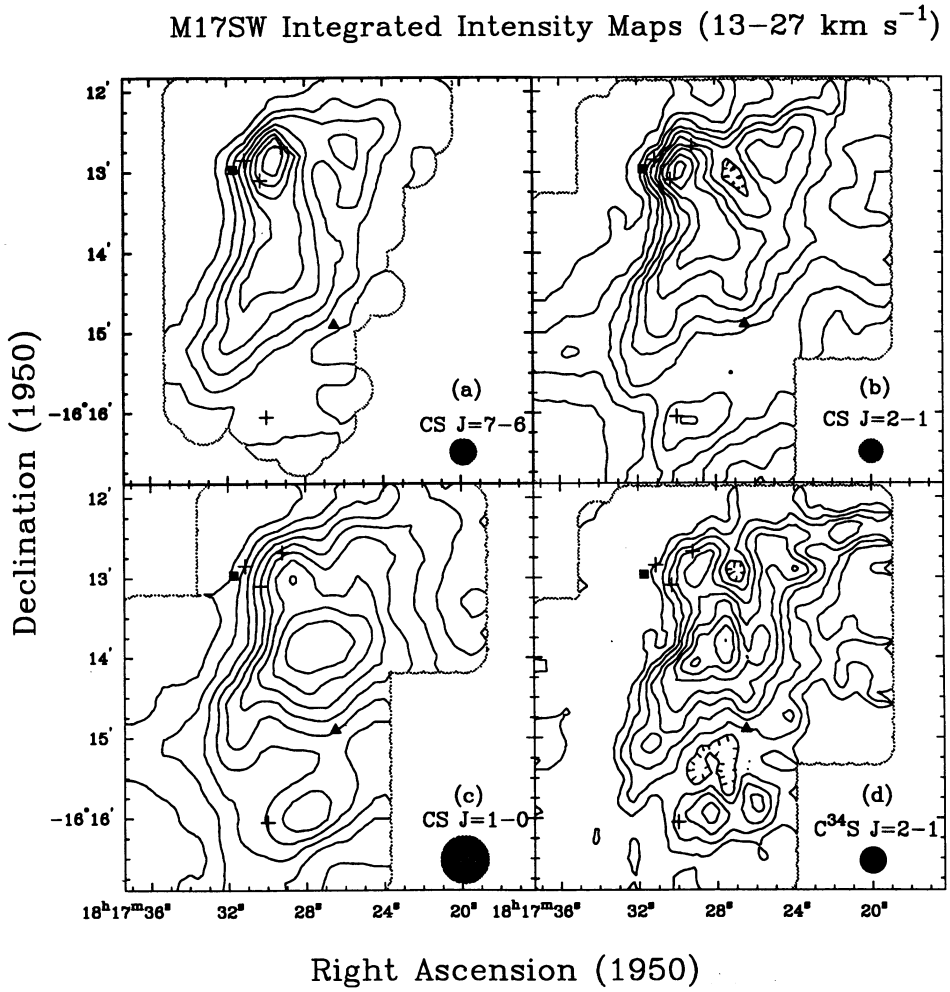

FIG. 2.—Velocity-integrated maps of CS and $C^{34}S$ lines from 13 km s^{-1} to 27 km s^{-1} plotted on a T_A^* scale defined in § 2. The crosshatched circle in each panel represents the half-power beamwidth. (*a*) CS $J = 7 \rightarrow 6$ line. The lowest contour and the contour spacing is 5.0 K km s^{-1}, and the 1 σ noise is 0.60 K km s^{-1}. The filled square, filled triangle, and four crosses are the same as described in Fig. 1. (*b*) CS $J = 2 \rightarrow 1$ line. The lowest contour and the contour spacing is 6.0 K km s^{-1} and the 1 σ noise is 0.84 K km s^{-1}. (*c*) CS $J = 1 \rightarrow 0$ line. The lowest contour and the contour spacing is 6.0 K km s^{-1}, and the 1 σ noise is 0.40 K km s^{-1}. (*d*) $C^{34}S$ $J = 2 \rightarrow 1$ line. The lowest contour and the contour spacing is 2.2 K km s^{-1}, and the 1 σ noise is 0.47 K km s^{-1}.

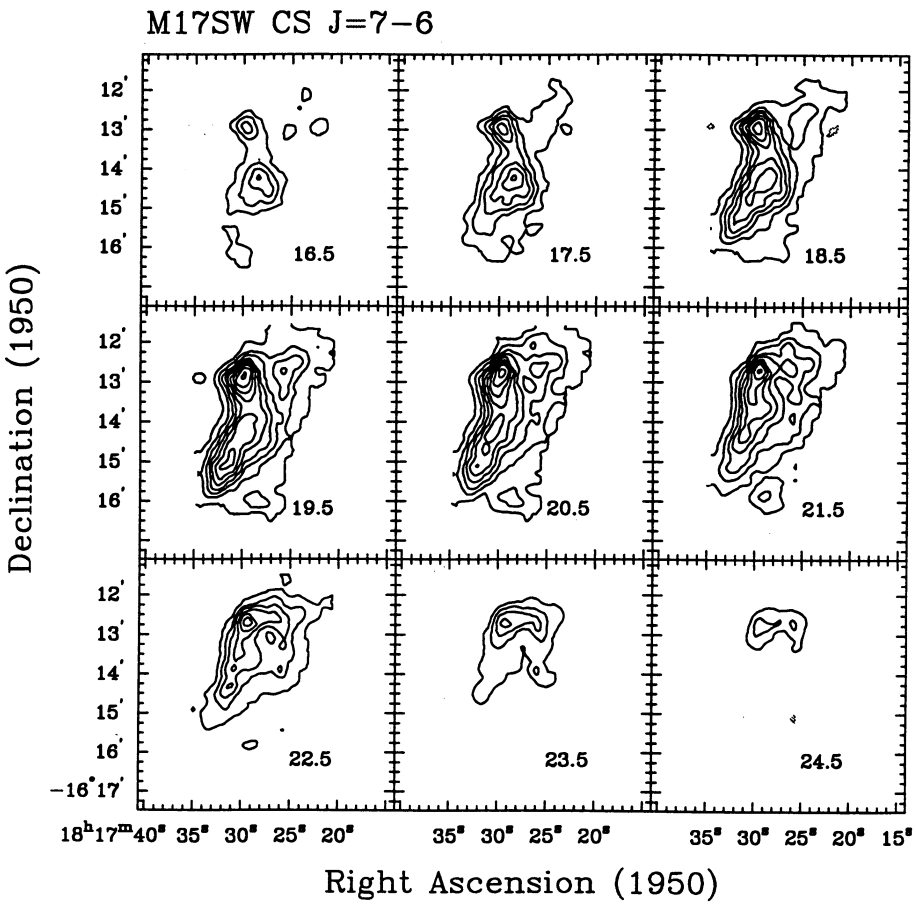

FIG. 3.—Velocity channel maps of CS $J = 7 \rightarrow 6$. The label in each panel gives the central velocity for the 1 km s^{-1} wide bin. The lowest contour and the contour spacing in each panel is 0.80 K km s^{-1}. The 1 σ noise is 0.14 K km s^{-1}.

Fiebig 1988). An additional condensation west of the hole (the "northwest condensation" in Fig. 1*c*) also appears in most of the velocity channels. In the CS $J = 2 \rightarrow 1$ channel maps (Fig. 4), there is an extended feature in the south (the "southern condensation" in Fig. 1*b*) with $V_{LSR} = 16$–18 km s^{-1}, which is isolated from the bulk of the CS emission, but seems to be associated with an H_2O maser. Another condensation appears in the southeast (Fig. 1*d*), beyond the edge of the CS $J = 7 \rightarrow 6$ map, with $V_{LSR} = 22$–24 km s^{-1}.

The morphology of the CS $J = 1 \rightarrow 0$ integrated intensity map (Fig. 2*c*) differs notably from the maps of higher J CS transitions (Figs. 2*a* and 2*b*). The CS $J = 1 \rightarrow 0$ map peaks toward the central condensation rather than at the northern condensation. This difference could result from density variations across the region with the CS $J = 1 \rightarrow 0$ emission arising mostly in the lower density ($\lesssim 10^4$ cm^{-3}) or intermediate-density gas (10^{4-5} cm^{-3}), while the transitions from higher J levels originate mainly from the high-density ($\gtrsim 10^5$ cm^{-3}) gas. Another possibility is that the difference results from optical depth effects. Excitation analysis (see § 4) shows that the CS $J = 1 \rightarrow 0$ line has a much lower opacity than the higher J CS lines at the densities and column densities that occur in M17 SW. If the prominent central condensation seen in the less opaque CS $J = 1 \rightarrow 0$ line represents a column density peak, the higher J lines would be optically thick there. Comparisons of the CS and C^{34}S $J = 2 \rightarrow 1$ profiles (see § 3.3) at the central condensation confirm that optical depth is the main effect. Opacity effects, however, cannot explain all the morphological differences between the CS $J = 1 \rightarrow 0$ and the higher J CS maps. While the northwestern condensation and the southern part of the ridge have the same relative strengths in all three CS maps, the northern condensation is relatively weak in CS $J = 1 \rightarrow 0$ line. Analysis of the CS and C^{34}S spectra implies that excitation effects may play a role in these particular morphological differences.

3.2. C^{34}S *Mapping Results*

The integrated intensity map of the C^{34}S $J = 2 \rightarrow 1$ line (Fig. 2*d*) agrees well with the C^{34}S $J = 3 \rightarrow 2$ map of Stutzki & Güsten (1990) over the smaller area where the $J = 3 \rightarrow 2$ line was mapped. The strongest emission in the C^{34}S $J = 2 \rightarrow 1$ map comes from the central condensation, confirming that the central condensation is a column density peak. Most of the features in the CS channel maps are also obvious in the C^{34}S channel maps (Fig 5). The central condensation dominates the C^{34}S emission for $V_{LSR} \lesssim 19$ km s^{-1}, while the northern condensation and the bright ridge are seen most clearly at 19–22 km s^{-1}. Features with $V_{LSR} \gtrsim 22$ km s^{-1} are relatively weak in the C^{34}S channel maps, but correspond to features seen in the CS $J = 2 \rightarrow 1$ and $7 \rightarrow 6$ channel maps. The less opaque C^{34}S channel maps *appear* lumpier than the more opaque CS maps, but some of this lumpiness is noise. If plotted with a contour step of 6 σ, similar to that used for the other maps, the C^{34}S maps are *not* lumpier than the CS maps. We conclude that with

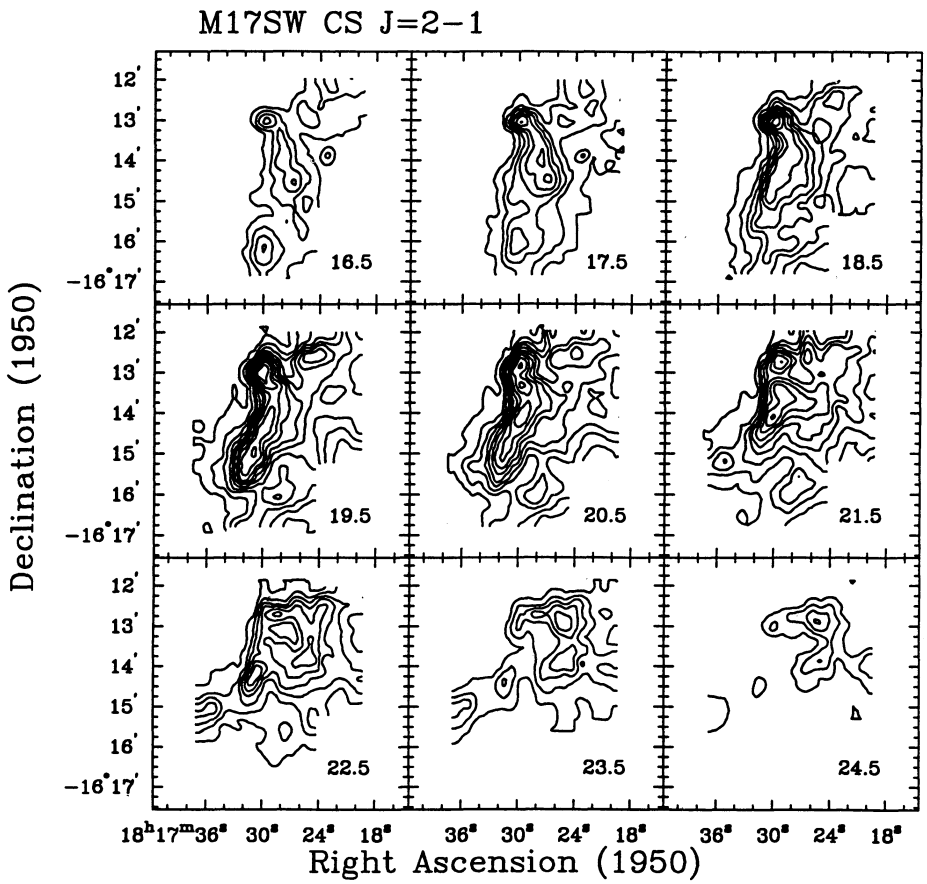

FIG. 4.—Velocity channel maps of CS $J = 2 \rightarrow 1$. The label in each panel gives the central velocity for the 1 km s^{-1} wide bin. The lowest contour and the contour spacing in each panel is 1.0 K km s^{-1}. The 1 σ noise is 0.18 K km s^{-1}.

a few exceptions, the opacity of the CS lines does not obscure the cloud structure.

The differences in the maps of different CS and C^{34}S lines imply variations in excitation and line opacity on scales of $\sim$20″–60″ (0.2–0.6 pc). The CS and C^{34}S channel maps (Figs. 3, 4, and 5) imply that the dense gas is clumpy on scales as small as our smallest beam size ($\sim$0.2 pc). The apparent morphological changes over velocity intervals of $\sim$1 km s^{-1} suggest that at least some substructures have intrinsic linewidths on the order of $\sim$1–2 km s^{-1}.

3.3. CS *and* C^{34}S *Line Profiles*

The peak CS and C^{34}S line temperatures in our maps are substantially higher than those in previous observations of M17 SW with lower spatial resolution (Snell et al. 1984; Mundy et al. 1986; Evans et al. 1987). Obviously, the lower resolution observations were affected by beam dilution. As a check of our calibration, we smoothed our data to a 60″ beam and compared the result to the previous spectra at the same locations. The resulting T_{mb} agreed with the previous observations to within $\pm$30% for the CS $7 \rightarrow 6$ line and to within $\pm$15% for the C^{34}S $2 \rightarrow 1$ line.

Although the critical densities for the CS $J = 7 \rightarrow 6$ and $J = 2 \rightarrow 1$ lines differ by two orders of magnitude, the lines have remarkably similar profiles. The ratio of the two lines, and the corresponding ratio for C^{34}S, across the spectral profiles show no indications of significant excitation variations with velocity. Based on the similar line profiles of the CO $J = 3 \rightarrow 2$ and $J = 1 \rightarrow 0$ lines, Martin, Sanders, & Hills (1984) proposed a macroturbulent model for the M17 SW cloud. Our data are consistent with a macroturbulent cloud in which the CS emission arises from unresolved, randomly moving substructures within the telescope beam (Zuckerman & Evans 1974). The linewidths in our 20″ observations are $\sim$80% of those seen in the 60″ beams of Evans et al. (1987), also consistent with a macroturbulent cloud, as long as most of the substructures are still smaller than 20″.

A single Gaussian profile can fit most of the CS and C^{34}S spectra in M17 SW quite well with the exception of a few locations. Near the northern condensation, both CS and C^{34}S lines exhibit strong and broad profiles (FWHM $\sim$5 km s^{-1}) superposed on even broader ($\gtrsim$10 km s^{-1} at the 1 K level for the CS $J = 7 \rightarrow 6$ line) line wings (Fig. 6*a*). The ridge at the interface has narrower ($\sim$2.5 km s^{-1}), Gaussian profiles with peak line temperatures comparable to those toward the northern condensation (Fig. 6*b*). The profiles near the central condensation are more complicated (Fig. 6*c*). CS $J = 2 \rightarrow 1$ line profiles are double-peaked at several locations near the central condensation. Since the C^{34}S $J = 2 \rightarrow 1$ lines are not strongly peaked at the central dip, we interpret the double-peaked profiles as two distinct kinematic components at $V_{LSR} \sim 18.5$ km s^{-1} and at $V_{LSR} \sim 21.5$ km s^{-1}. In fact, the observed CS and C^{34}S lines toward the central condensation are all consistent with the two-component model (Fig. 6*c*). This interpretation is also consistent with the multitransition NH_3 data (Güsten & Fiebig 1988), in which all NH_3 inversion lines [$(J, K) = (1, 1)$ to

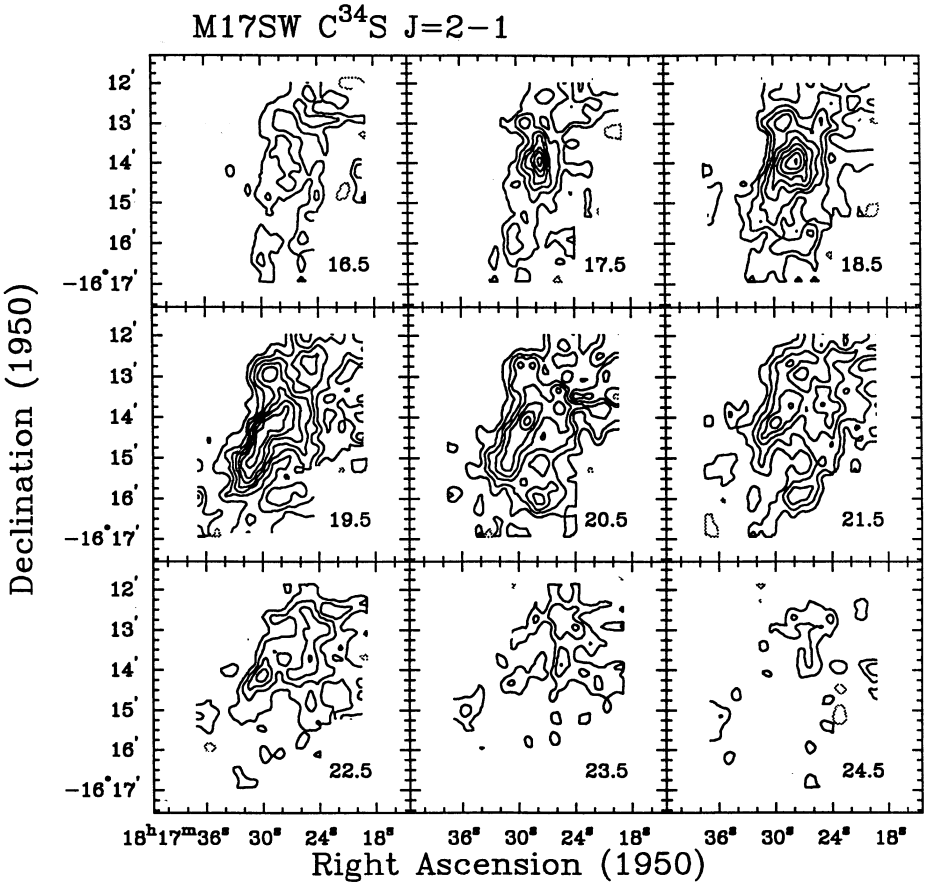

FIG. 5.—Velocity channel maps of $C^{34}S$ $J = 2 \rightarrow 1$. The label in each panel gives the central velocity for the 1 km s^{-1} wide bin. The lowest contour and the contour spacing in each panel is 0.25 K km s^{-1}. Dashed lines indicate negative contours. The 1 σ noise is 0.12 K km s^{-1}.

(5, 5)] have peaks at $V_{LSR} \sim 19.0$ km s^{-1} and $V_{LSR} \sim 21.8$ km s^{-1} near the central condensation. Assuming equal excitation temperatures for the $J = 2 \rightarrow 1$ lines of CS and $C^{34}S$ and an abundance ratio of 22 for $C^{32}S$ to $C^{34}S$, we estimate the CS $J = 2 \rightarrow 1$ optical depths to be ~ 6 at $V_{LSR} \sim 18.5$ km s^{-1} and ~ 2 at $V_{LSR} \sim 21.5$ km s^{-1}. The optical depth estimate confirms our earlier conclusion that the central condensation is a column density peak and that the higher J CS lines are moderately opaque at this peak.

4. THE DENSITY STRUCTURE OF M17 SW

4.1. *Results of a Simple Analysis*

What do the local maxima in the CS maps represent? Since they agree roughly with the emission peaks seen in the $C^{18}O$ maps of Stutzki & Güsten (1990), it is natural to assume that peaks in the CS maps represent density enhancements corresponding to the clumps identified by those authors. We will test this hypothesis by a simple analysis of our data to identify local density peaks.

The underlying assumption of our method for determining the local gas density (n) is that collisions compete with radiative transitions to establish the excitation of CS. Because higher density increases the populations in the higher J levels of CS, the ratio of the $J = 7 \rightarrow 6$ emission to the $J = 2 \rightarrow 1$ emission [hereafter R(7–6/2–1)] should increase with gas density. Indeed, Evans et al. (1987) demonstrated that R(7–6/2–1) is primarily a density probe over a wide range of CS column density [up to $N(CS)/\Delta v \approx 10^{14.5}$ cm^{-2} (km s^{-1})$^{-1}$].

If the CS emission peaks correspond to density enhancements, R(7–6/2–1) should increase with line intensity. In fact, there is no such trend in the data (Fig. 7). Although the intensities of both the CS $J = 7 \rightarrow 6$ and $2 \rightarrow 1$ lines increase by a factor $\gtrsim 10$ from cloud edges to the peaks in M17 SW, almost all the line ratios are consistent with a random distribution about an average R(7–6/2–1) = 0.41, considering the calibration and statistical uncertainties. This result suggests that maps of single molecular transitions, even of transitions with high critical densities, do not necessarily trace local density. Therefore, the conventional identification of the intensity peaks in molecular line maps as cores or clumps, with the implicit assumption that these regions have higher density than their surroundings, is not always correct. We will therefore use an excitation analysis to produce a density map of M17 SW.

After describing the method of analysis, we will use the CS $J = 7 \rightarrow 6$ and $J = 2 \rightarrow 1$ lines to obtain the density distribution. We will evaluate the validity of these results by including more transitions of CS at selected positions. We will then use the optically thin $C^{34}S$ $J = 7 \rightarrow 6$, $J = 3 \rightarrow 2$, and $2 \rightarrow 1$ lines to obtain independent estimates of the gas densities and $C^{34}S$ column densities along two cuts across the core, compare the results with those obtained with the CS lines, and discuss the possible sources of uncertainties in the analysis.

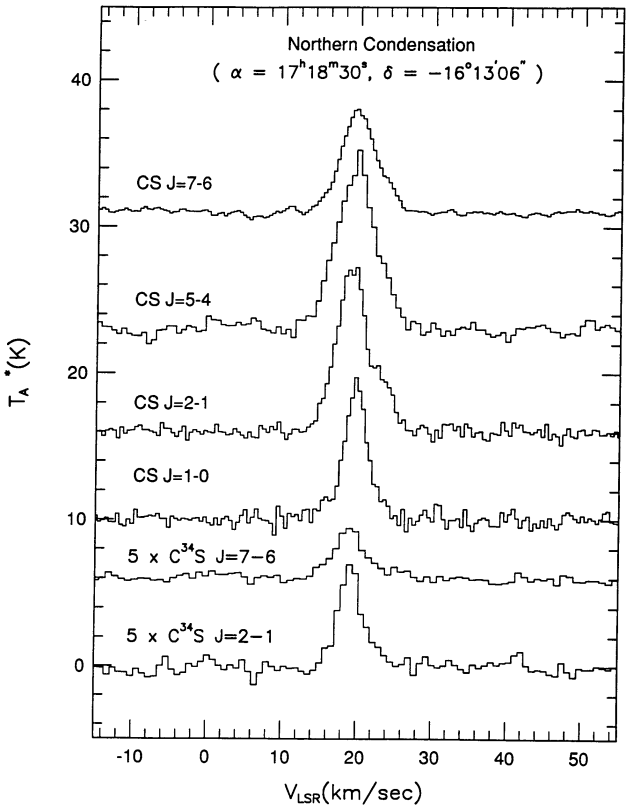

FIG. 6*a*

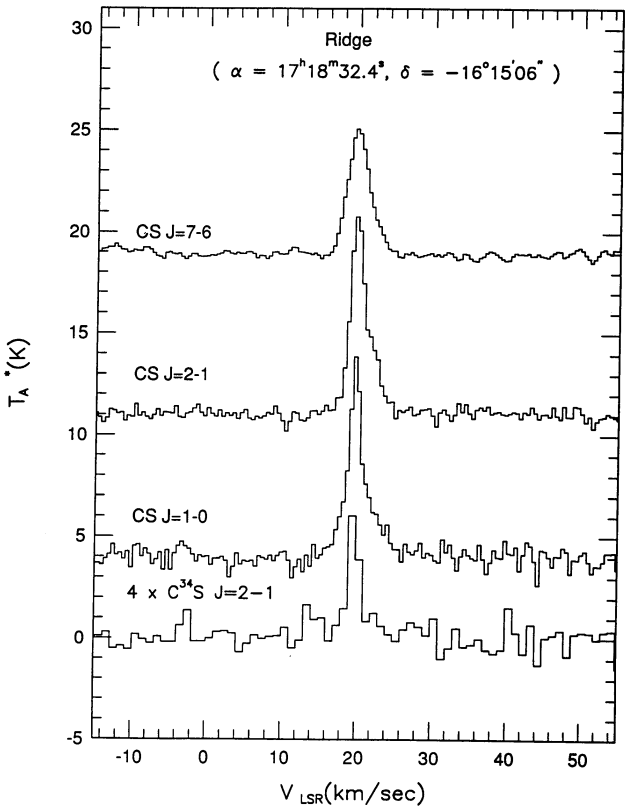

FIG. 6*b*

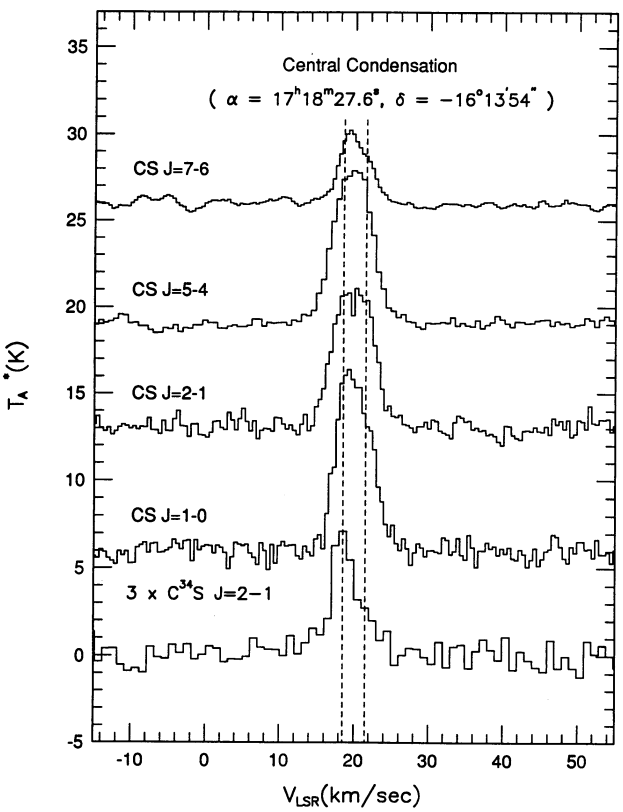

FIG. 6*c*

4.2. *Method of Analysis: Fitting to LVG Models*

In cases when photon trapping is important, line ratios no longer yield a unique value of density. Coupled modeling of molecular excitation and radiative transport is needed to derive the volume density and column density. The large velocity gradient (LVG) model (Scoville & Solomon 1974; Goldreich & Kwan 1974; De Jong, Chu, & Dalgarno 1975) is the most widely used radiative transfer model, due largely to its simplicity and the small number of free parameters. Although there is no evidence for a smooth velocity gradient in M17 SW and the structure is clumpy, the LVG model accounts for photon trapping effects to first order. More important, it gives results which are not very different from the results of microturbulent and other radiative transfer models, as long as the optical depths are not too large (Liszt & Leung 1976; White 1976). Comparisons of results from LVG and microturbulent models indicate that differences between the parameters derived from the two models are about a factor of 3, comparable to those resulting from the uncertainties in the geometry of the observed clouds (White 1976; Snell 1981).

We adopted the same LVG code used by Snell et al. (1984), which assumes a spherical cloud with uniform density and kinetic temperature, with velocity proportional to the radius.

FIG. 6.—Line profiles of CS and $C^{34}S$. (*a*) Profiles near the northern condensation at R.A. = $17^h18^m30^s.0$ and decl. = $-16°13'06''$. (*b*) Profiles in the ridge at R.A. = $17^h18^m32^s.4$ and decl. = $-16°15'06''$. (*c*) Profiles near the central condensation at R.A. = $17^h18^m27^s.6$ and decl. = $-16°13'54''$. The two dashed vertical lines mark V_{LSR} = 18.5 km s^{-1} and V_{LSR} = 21.5 km s^{-1}, respectively.

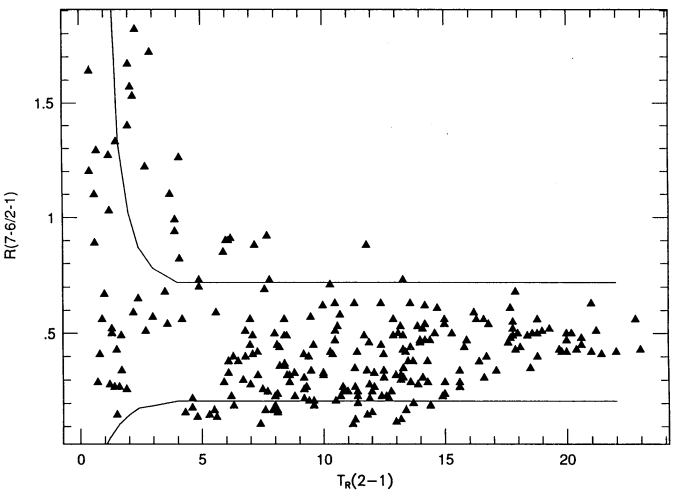

FIG. 7.—The ratio of the CS $J = 7 \rightarrow 6$ and $J = 2 \rightarrow 1$ peak temperatures [$R(7\text{–}6/2\text{–}1)$] vs. the CS $J = 2 \rightarrow 1$ line temperature [$T_R(J = 2 \rightarrow 1)$]. The two lines in the plot represent $R(7\text{–}6/2\text{–}1) = 0.41 \pm 2\,\sigma$, where σ is the uncertainty of the ratio determined by both the statistical errors of the measurement (rms) and the calibration uncertainties of both lines (20% for the $7 \rightarrow 6$ line and 10% for the $2 \rightarrow 1$ line).

The collisional rates for CS were taken from Green & Chapman (1978). The peak opacity is proportional to the molecular column density per unit velocity interval ($N/\Delta v$). The analysis thus yields the best-fit gas density and CS column density per unit velocity interval for a given gas temperature (T_K). In the procedure, each line of sight was treated independently and the global structure of the cloud was neglected. The density is effectively averaged over the telescope beam and along the line of sight, but weighted toward denser regions (Snell et al. 1984). The derived column density assumes that the telescope beam is filled with gas of uniform density. For a clumpy cloud, the "column density" derived from this method depends on a combination of the actual column density and the beam-filling factor.

LVG modeling requires knowledge of T_K. Far-IR continuum and multitransition NH_3 studies show that M17 SW is heated externally by OB stars east of the core (Wilson et al. 1979; Gatley et al. 1979; Güsten & Fiebig 1988). Since the bulk of the dense gas has temperatures determined from NH_3 of 50 ± 15 K, we assume a uniform $T_K = 50$ K.

The CS data were analyzed by comparing the peak temperatures of the $J = 7 \rightarrow 6$ and $2 \rightarrow 1$ lines to a grid of LVG models to obtain the best-fit density and CS column density at each position where both transitions were observed. The best fit was determined by minimizing χ^2, which is defined as

$$\chi^2 = \sum \{[T_R(\text{model}) - T_R(\text{obs})]/\Delta T_R(\text{obs})\}^2 ,$$

where the summation is performed over all transitions used in the fit, T_R(model) is the model line temperature from the LVG calculation, T_R(obs) is the observed line temperature, and ΔT_R(obs) the uncertainty in T_R(obs), including both the calibration uncertainties and the statistical errors. We assumed a calibration uncertainty of 20% for the CSO observations and 10% for the NRO observations. The statistical errors were derived from the noise in the baselines of the observed spectra.

4.3. CS *Results: Density and Column Density Maps of M17 SW*

In order to preserve high spatial resolution while covering a large area, we used only the two fully sampled maps of the core (CS $J = 2 \rightarrow 1$ and $J = 7 \rightarrow 6$) to obtain maps of density (n) and "column density" [$N(\text{CS})/\Delta v$] with 252 pixels (Fig. 8).

The gas density ranges from 1.6×10^5 to 2.5×10^6 cm^{-3}; the lowest density points are found near the western edge of the map. The densities above 1.0×10^6 cm^{-3} are all in the extreme northeast, where our assumption that $T_K = 50$ K causes us to overestimate the density (see § 4.5.2). The CS column density, calculated by multiplying $N/\Delta v$ from the models by the average FWHM of the $J = 7 \rightarrow 6$ and $2 \rightarrow 1$ lines, varies from $\sim 1.5 \times 10^{13}$ cm^{-2} near the east rim of the core to $\sim 1.8 \times 10^{15}$ cm^{-2} toward the strongest condensations. At most positions the density is between $3\text{–}6 \times 10^5$ cm^{-3} and N(CS) is between 1.5×10^{14} and 1.5×10^{15} cm^{-2}. The densities we obtained are close to those obtained by Snell et al. (1984), while our CS column densities are higher by a factor of 2–3. Stutzki & Güsten (1990) analyzed more limited CS and $C^{34}S$ data at one position near the northern condensation, finding a density of at least 10^6 cm^{-3}, about twice the density we obtained at the same location. The difference is probably a result of different assumptions about radiative transport (see § 4.5.1).

With an improvement in angular resolution by a factor of 3 over earlier CS observations (Snell et al. 1984), our maps show considerably more structure. However, peaks in the line temperature maps, even of "high-density" tracers like CS $J = 7 \rightarrow 6$, do not appear as density enhancements in Figure 8, as suggested by our simple analysis. In this case, the line temperatures of CS and $C^{34}S$ transitions are likely to be measures of the beam-filling factor of the unresolved substructures. Except for the arc-shaped feature in the extreme northeast, which may be an artifact of assuming constant T_K, the density distribution is remarkably featureless, with $n \sim 10^{5.7 \pm 0.2}$ cm^{-3} in most of the mapped area.

In contrast to the density map, the column density map corresponds closely with peak line temperature maps of the CS and $C^{18}O$ lines, showing a ridge of $N(\text{CS})/\Delta v$ along the interface with the H II region. The edge-on geometry of M17 SW makes it tempting to speculate that the ridge is gas compressed by a shock preceding the ionization front into the cloud, setting the stage for the next generation of star formation (Elmegreen & Lada 1977). However, while the ridge is a column density peak, there is no indication of a density enhancement within the ridge as compared to the other parts of the core. Therefore, the "ridge" cannot be simply identified as the swept-up postshock layer. In addition, such ridgelike structures are also seen in other sources in which the ridges are not always parallel to the ionization fronts, such as in NGC 2024 (Schulz et al. 1991), Orion A (Genzel & Stutzki 1989), and DR 21/W75S (Wilson & Mauersberger 1990). It is more likely that these ridgelike features are filaments or bundles of filaments and clumps with a filamentary geometry and a higher filling factor of dense material than surrounding regions, rather than sheetlike structures seen edge-on. The causes and the supporting mechanisms of such large-scale filaments are not clear, but it will be important to establish whether they actually have enhanced densities. The ridge could also be the only remnant of the high column density part of the cloud which formed the star cluster which now ionizes the H II region.

Within the typical density and CS column density ranges, the $J = 2 \rightarrow 1$ and $J = 7 \rightarrow 6$ transitions of CS have modest optical depths ($\tau_{2\rightarrow1} \sim 1$ and $\tau_{7\rightarrow6} \sim 3$). While optical depths are accounted for, to first order, by the LVG model, self-absorption effects are not; these could cause systematic errors

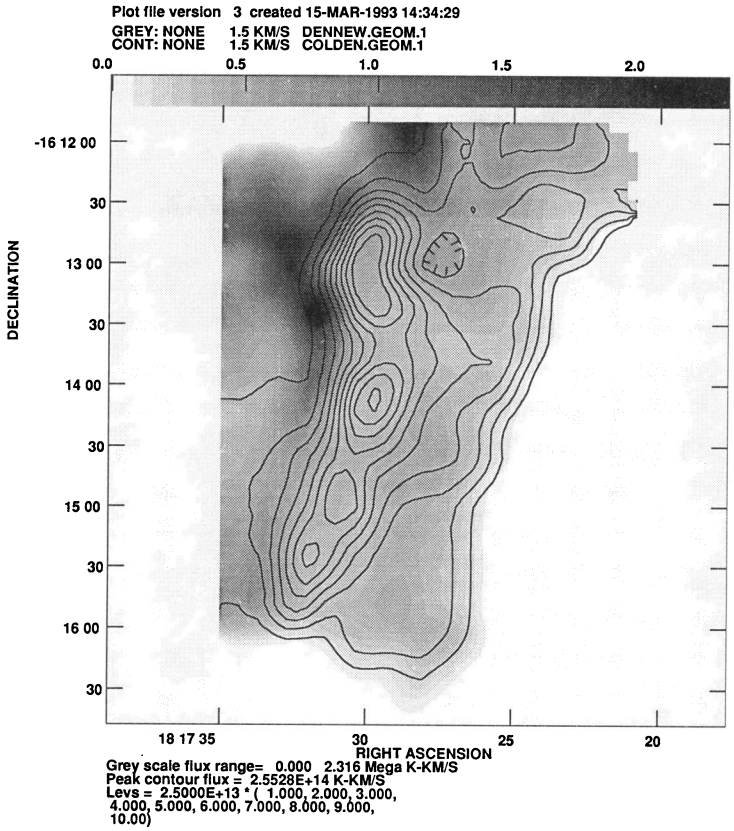

FIG. 8.—Maps of gas density and CS column density in M17 SW derived from the CS $J = 7 \rightarrow 6$ and $J = 2 \rightarrow 1$ lines. Density is plotted in a linear gray scale ranging from 1.0×10^5 cm^{-3} to 2.3×10^6 cm^{-3}. The contours are the CS column density ($N/\Delta v$) distribution. The lowest contour and the contour spacing is 2.5×10^{13} cm^{-2} (km s^{-1})$^{-1}$.

in the density and column density maps. The CS $J = 1 \rightarrow 0$ line has lower optical depth ($\tau \lesssim 0.4$) than the other transitions, partly because it is usually suprathermally excited, in the parameter space that fits the CS observations. The models thus confirm our earlier conclusion that opacity effects can explain some of the morphological differences between the CS $J = 1 \rightarrow 0$ map and the maps of the higher J lines.

We compared the results of the LVG models using the CS $J = 2 \rightarrow 1$ and $J = 7 \rightarrow 6$ lines with the observed CS $J = 1 \rightarrow 0$ and $J = 5 \rightarrow 4$ lines. Considering that the CS $J = 1 \rightarrow 0$ and $5 \rightarrow 4$ lines were observed with larger ($\sim 30''$) beams, we found reasonable agreement between the line temperatures predicted by the best-fit LVG models for the CS $J = 2 \rightarrow 1$ and $7 \rightarrow 6$ lines and the observed $1 \rightarrow 0$ and $5 \rightarrow 4$ lines. Figure 9 shows T_R versus $J_{\rm upper}$ for two examples, with the best-fit LVG models based on the CS $J = 2 \rightarrow 1$ and $7 \rightarrow 6$ data alone (*solid lines*) and all the observed CS lines. For positions where all four lines were observed we fitted the LVG models to the four lines (*dashed lines*) and found that the simple, uniform density LVG model could fit the observed data well: $\chi^2 \sim 1$–3 for most of these positions; in the worst cases, $\chi^2 \sim 5$–6. The parameters from fitting all four lines are not much different (± 0.2 in log scale) from those using only the $J = 2 \rightarrow 1$ and $J = 7 \rightarrow 6$ lines.

4.4. $C^{34}S$ *Results*

The $C^{34}S$ lines are much less opaque ($\tau \lesssim 0.2$) than the CS lines in the density and column density range of the fits to the CS data and therefore should suffer much less from self-absorption. We apply the same procedure used for the CS lines to the $C^{34}S$ $J = 2 \rightarrow 1$, $J = 3 \rightarrow 1$, and $J = 7 \rightarrow 6$ lines to obtain independent estimates of the gas density. The $C^{34}S$ $J = 7 \rightarrow 6$ spectra were observed along two cuts through M17 SW: one in declination through the northern and the central condensations, and one in right ascension from the ionization front in the east through the ultracompact H II region and the northern condensation. The $C^{34}S$ $J = 3 \rightarrow 2$ spectra (Stutzki & Güsten 1990) were observed with a 17″ beam, on a different grid, with about 20″ spacings. We used a linear interpolation scheme to place them on our grid, assuming an error of $\pm 30\%$ for the peak temperatures to account for additional uncertainties introduced by the interpolation.

The densities derived from the $C^{34}S$ and CS transitions agree very well {log [n(CS)] = log [$n(C^{34}S)$] $\pm$ 0.12} (Figs. 10 and 11). The average ratio of N(CS)/$N(C^{34}S)$ is 13.2 $\pm$ 5.2 (Fig. 11). The column density ratio shows an interesting trend along the declination scan. The ratio near the northern condensation is close to the terrestrial $^{32}S/^{34}S$ ratio of 22.5, but it decreases by a factor of 2 to the south. The decreasing N(CS)/$N(C^{34}S)$ ratio to the south may be caused by an underestimation of N(CS) near the central condensation due to the large CS opacities. Furthermore, if the emitting gas is clumpy on scales smaller than the telescope beams, the LVG fitting underestimates N(CS) more than it does $N(C^{34}S)$ (Mundy et al. 1986).

For most of the observed positions, the fits are good. with $\chi^2 \lesssim 2$. Figure 12 shows two examples of the best-fit LVG models along with the observed line intensities. For most of the bad fits, the model predicts $J = 3 \rightarrow 2$ line temperatures that are systematically stronger than the observed temperatures

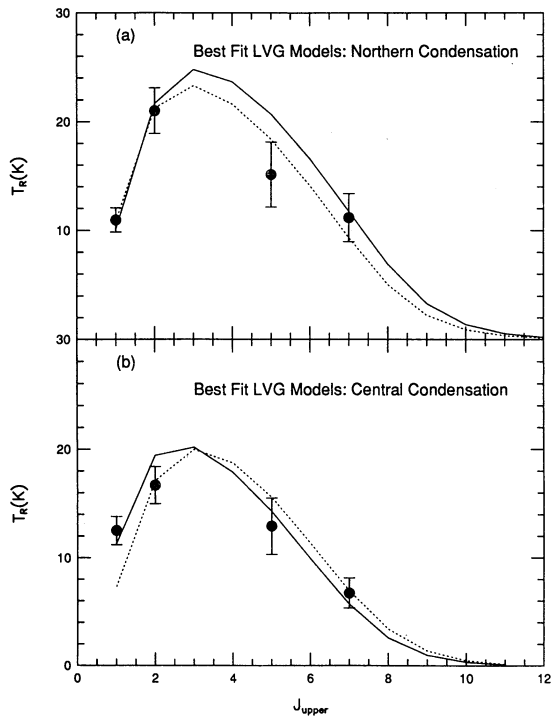

FIG. 9.—The best-fit LVG models compared with the observed $J = 1 \rightarrow 0$, $2 \rightarrow 1$, $5 \rightarrow 4$, and $7 \rightarrow 6$ lines. (*a*) The comparison at R.A = $17^h18^m30^s.0$ and decl. = $-16°13'06''$ (the northern condensation). The solid line represents the best fit from $J = 7 \rightarrow 6$ and $J = 2 \rightarrow 1$ lines ($n = 10^{5.66}$ cm^{-3}, $N/\Delta v = 10^{14.40}$ cm^{-2} [km s^{-1}]$^{-1}$ and the dashed line is the best fit from all four lines ($n = 10^{5.54}$ cm^{-3}, $N/\Delta v = 10^{14.40}$ cm^{-2} [km s^{-1}]$^{-1}$). (*b*) The comparison at R.A. = $17^h18^m27^s.6$ and decl. = $-16°13'54''$ (the central condensation). The solid line represents the best fit from $J = 7 \rightarrow 6$ and $J = 2 \rightarrow 1$ lines ($n = 10^{5.62}$ cm^{-3}, $N/\Delta v = 10^{14.20}$ cm^{-2} [km s^{-1}]$^{-1}$ and the dashed line is the best fit from all four lines ($n = 10^{5.37}$ cm^{-3}, $N/\Delta v = 10^{14.36}$ cm^{-2} [km s^{-1}]$^{-1}$).

while the model predicts $C^{34}S$ $J = 2 \rightarrow 1$ line temperatures weaker than those observed. These bad fits may imply that density inhomogeneities exist along these lines of sight and that the single density LVG model is not adequate for these positions.

The good agreement between the densities derived independently from the less opaque $C^{34}S$ lines and from the CS lines confirms the conclusions based only on CS data. As a further consistency check, we fitted the CS data and $C^{34}S$ data simultaneously by assuming a global CS/$C^{34}S$ ratio. Along the declination cut, the best-fit densities and CS column densities including the $C^{34}S$ lines agree well (to within ± 0.3 in log scale) with those obtained from the CS data and are only weakly dependent on the assumed isotopic ratio. At most of the positions along the cut, an isotopic ratio of 13 results in smaller values for the combined χ^2's than those obtained assuming a terrestrial isotopic ratio, consistent with the average isotopic ratio derived from the CS and $C^{34}S$ column densities.

4.5. *Systematic Uncertainties*

Snell et al. (1984) and Mundy et al. (1986) have discussed in detail the major sources of uncertainty in an LVG analysis. We briefly discuss the situation for the particular transitions that we have used.

4.5.1. *The Radiative Transfer Model*

To isolate the effect of the assumed velocity field on the derived parameters, we compared two extreme cases of velocity fields, i.e., the LVG assumption [specifically $v(r) \propto r$] and the microturbulent velocity field. We computed a series of microturbulent models of isothermal, uniform density spheres as model clouds and then convolved the emergent line intensities with Gaussian telescope beams to obtain model line temperatures. The resulting T_R's of the CS and $C^{34}S$ $J = 7 \rightarrow 6$ and $2 \rightarrow 1$ lines as functions of projected cloud radius were then fitted with the same LVG grid used in our fitting procedure. The comparison of the derived n and $N(CS)/\Delta v$ [or $N(C^{34}S)/\Delta v$] with the model values then tests the effect of assumed velocity field on the derived parameters.

We found good agreement between n and $N/\Delta v$ from the fits to the LVG code and the model values (within a factor of 2), as long as the column densities are not too large [$N(CS)/\Delta v \lesssim 10^{14.5}$ cm^{-2} (km s^{-1})]. Even in the worst cases, with large CS column densities, the best-fit gas density underestimates the model density by a factor of ~ 3–4. Figure 13 plots an example of the derived n and $N/\Delta v$ as a function of the projected radius for a spherical cloud with radius 0.25 pc and density $n = 5 \times 10^5$ cm^{-3} and $N(CS)/\Delta v = 10^{14.92}$ cm^{-2} (km s^{-1})$^{-1}$ through the cloud center. This is one of the larger column densities that we see, so this simulation should provide a worst case analysis. The $C^{34}S$ model was calculated by assuming an abundance ratio of 20 for the CS and $C^{34}S$. We found that the gas densities derived from CS lines and $C^{34}S$ lines may differ by a factor of 3–4 in the cloud center where the CS line opacities are large. This range includes the difference between our densities and those of Stutzki & Güsten at one position near the northern condensation (Stutzki & Güsten 1990). The best-fit gas density derived from the CS lines is systematically smaller than that derived from the $C^{34}S$ lines in these tests. The actual agreement between the CS best-fit densities and the

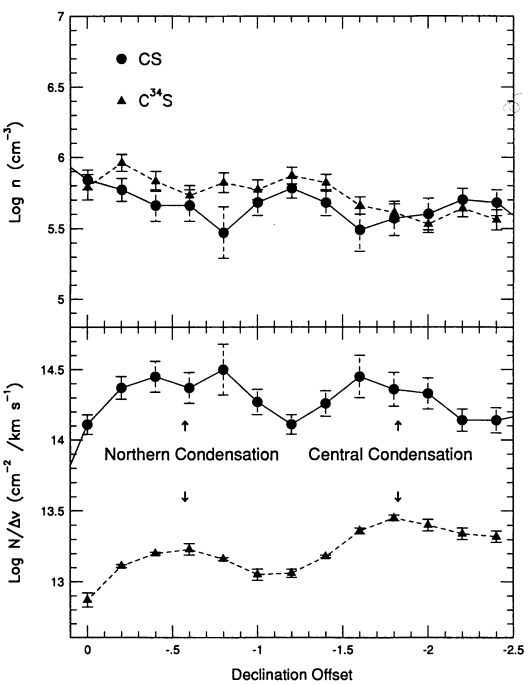

FIG. 10.—*Upper panel*: The gas density distribution derived from the CS (*dashed line*) and $C^{34}S$ (*solid line*) data along the declination scan at R.A. = $17^h18^m30^s.0$ through the peak of the northern condensation and partially through the central condensation. The (0, 0) position in the plot is ($17^h18^m30^s.0$, $-16°12'30''$). *Lower panel*: The comparison of the CS (*dashed line*) and $C^{34}S$ (*solid line*) column density distribution along the same scan.

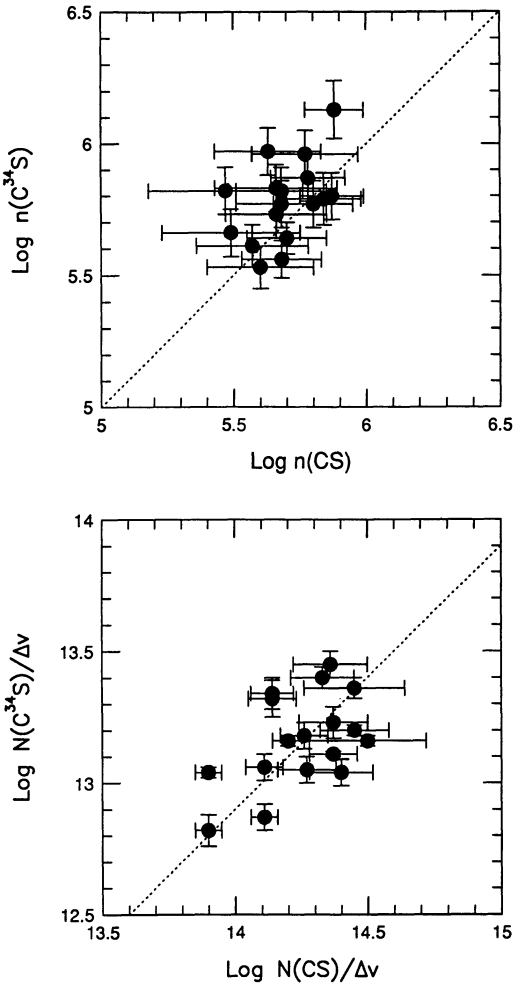

FIG. 11.—Comparisons of the densities and column densities derived from the CS lines and from the $C^{34}S$ lines. The upper panel plots the densities derived from the CS $J = 2 \rightarrow 1$ and $7 \rightarrow 6$ lines against the densities derived from the $C^{34}S$ $J = 2 \rightarrow 1$, $3 \rightarrow 2$, and $7 \rightarrow 6$ lines; the lower panel plots the CS column densities against the $C^{34}S$ column densities at the same locations. The dashed lines correspond to equal densities (*upper panel*) and a constant column density ratio $N(CS)/N(C^{34}S) = 13.2$ (*lower panel*).

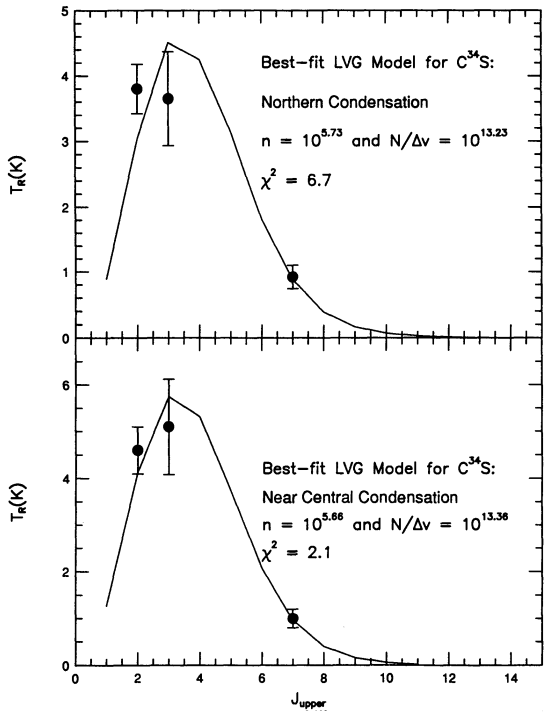

FIG. 12.—LVG models for the $C^{34}S$ observations compared with the observed $C^{34}S$ $J = 2 \rightarrow 1$, $3 \rightarrow 2$, and $7 \rightarrow 6$ lines. The upper panel gives the best-fit model at R.A. = $17^h18^m30^s.0$ and decl. = $-16°13'06''$ (northern condensation). The lower panel gives the best-fit model at R.A. = $17^h18^m30^s.0$ and decl. = $-16°14'06''$ (central condensation).

$C^{34}S$ best-fit densities in M17 SW therefore is significant, demonstrating that optical depth effects are not a serious problem and confirming the conclusions based only on the CS transitions.

4.5.2. *The Effect of Kinetic Temperature*

From their multitransition NH_3 study, Güsten & Fiebig (1988) noticed a slow fall-off of kinetic temperature away from the ionization front to the southwest (see also Gatley et al. 1979). Over the $3' \times 4'$ region we observed, the kinetic temperature typically (the region of the northern condensation is a notable exception) decreases from ~ 55 K near the front to ~ 25 K about 2′ southwest of the front. Because of the edge-on geometry of the region, the temperature gradient is most likely perpendicular to the line of sight. Thus it is relatively easy to evaluate the effect of kinetic temperature variation on the derived parameters. We ran a series of LVG models with different kinetic temperatures and then fitted the CS $J = 7 \rightarrow 6$ and $2 \rightarrow 1$ lines to these models to derive gas density and CS column density.

Figure 14 shows an example, in which we fitted the typical

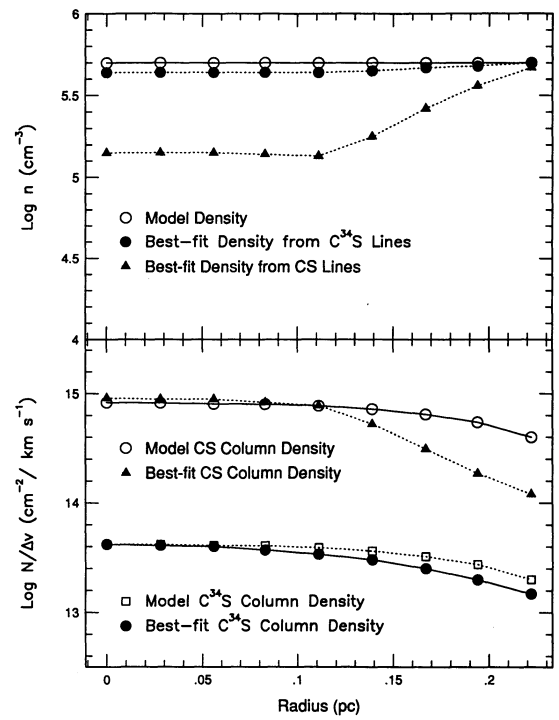

FIG. 13.—LVG fit to the CS and $C^{34}S$ line temperatures of a model microturbulent cloud with uniform density with radius of 0.25 pc, density of $10^{5.7}$ cm^{-3}, temperature of 50 K, and turbulent velocity width of 3 km s^{-1} (FWHM). Best-fit densities from the CS $J = 2 \rightarrow 1$ and $J = 7 \rightarrow 6$ lines and from the $C^{34}S$ $J = 2 \rightarrow 1$, $3 \rightarrow 2$, and $7 \rightarrow 6$ lines as functions of projected cloud radius are plotted in the upper panel; best-fit CS and $C^{34}S$ column densities are plotted in the lower panel.

observed values for the CS condensations in M17 SW [$T_R(2 \rightarrow 1) = 16$ K and $T_R(7 \rightarrow 6) = 8$ K] by LVG grids with different T_K from 20 K to 260 K. For a temperature range of a factor of 13, the derived density and column density vary by a factor of ~ 3–4 (~ 0.5 in log scale) (Fig. 14). Within the likely temperature range for most of M17 SW (20–60 K), the derived density and column density only differ by a factor of $\lesssim 1.5$ with the fractional uncertainties in the derived parameters comparable to the calibration uncertainties (error bars in Fig. 14 are obtained assuming 20% and 10% calibration uncertainties for $7 \rightarrow 6$ and $2 \rightarrow 1$ observations, respectively). We therefore conclude that our CS fitting results, with an assumed $T_K = 50$ K, should not be affected by T_K variations over most of the region. The only exception is the eastern rim of the northern condensation where our density map shows an arc of material with density significantly higher than 5×10^5 cm^{-3}. In the region right around the radio continuum arc, Güsten & Fiebig (1988) find evidence for a gas component with a temperature of ~ 275 K. Harris et al. (1987) detected CO $J = 14 \rightarrow 13$ and $J = 7 \rightarrow 6$ lines in the same region and derived a temperature of > 200 K. We tested the possibility that the density enhancement along the arc is a temperature artifact by fitting the observed line intensities of the arc with LVG grids at much higher temperatures and found that the density enhancement along the edge of the northern condensation disappears if T_K is ~ 200 K. Therefore, the high-excitation gas near the radio continuum arc may well be the warm ($\gtrsim 200$ K) molecular gas exposed to high far-ultraviolet fluxes along the interface (Harris et al. 1987). As a result, there is no place within our map where there is evidence for an enhancement in the volume density over a region larger than or equal to our beam. Further observations of the higher excitation CS lines (e.g., CS $J = 10 \rightarrow 9$ line, which is ~ 120 K above the ground state), which are more sensitive to temperature effects, would be desirable to understand the more highly excited gas near the ionization front.

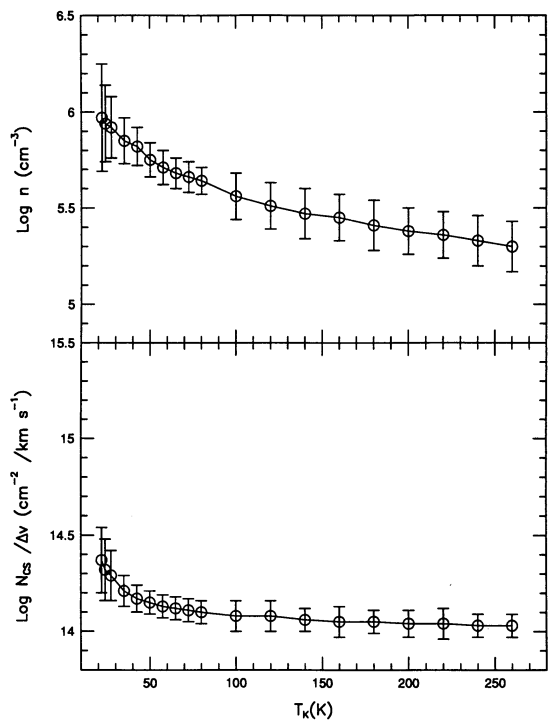

FIG. 14.—The temperature dependence of best-fit LVG densities and column densities derived from the CS $J = 7 \rightarrow 6$ and $2 \rightarrow 1$ lines. Error bars in the derived density and column density are determined assuming 10% uncertainty for the $J = 2 \rightarrow 1$ line and 20% uncertainty for the $J = 7 \rightarrow 6$ line.

4.5.3. *Effects of Density Inhomogeneities*

Snell et al. (1984) and Mundy et al. (1986) have investigated the effects of density inhomogeneities within the beam on LVG model results. They conclude that in a region with a mixture of high- and low-density gas, an LVG analysis will find a density close to that of the denser gas, as long as that gas has an area filling factor of > 0.2–0.4. Mundy et al. (1986) considered a specific two-component model with $n = 10^6$ cm^{-3} clumps immersed in an $n = 2 \times 10^3$ cm^{-3} interclump gas. They found that the density derived from LVG analysis is close to the clump density and depends only weakly on the clump filling factor for filling factors ≥ 0.4.

Our analysis is similar to that of Snell et al. and Mundy et al., except that, over most of M17 SW, we use only the CS $J = 2 \rightarrow 1$ and $7 \rightarrow 6$ lines, which have very different excitation requirements. Since these two lines may sample gases of very different densities, multiple densities within the telescope beams may cause systematic effects in the fits. Comparison of the best-fits of the LVG models based on the $J = 2 \rightarrow 1$ and $7 \rightarrow 6$ observations to the observed CS $J = 1 \rightarrow 0$ and $5 \rightarrow 4$ lines and the good agreement between the densities derived from the CS lines and those from the optically thin $C^{34}S$ lines indicate that, in spite of these worries, fits to only the $J = 2 \rightarrow 1$ and $J = 7 \rightarrow 6$ CS lines closely approximate the results obtainable with more transitions, or less opaque transitions.

4.6. *Summary*

Our analysis of the excitation of the CS emission with 20″ resolution has led to a conclusion similar to that of earlier work with 1′ resolution: significant density structure remains unresolved (< 0.2 pc). There is no evidence for smooth density gradients on scales above 0.2 pc. The simplest picture compatible with our data is that of a large number of dense clumps, mostly smaller than 0.2 pc, moving with velocity dispersion of a few km s^{-1}. Stutzki & Güsten (1990) have adopted just such a picture and deconvolved their higher resolution (13″) $C^{18}O$ map into 179 clumps. In the next section, we will consider whether their clumps can explain our data.

5. COMPARISON TO THE CLUMP MODEL OF STUTZKI AND GÜSTEN (1990)

Stutzki & Güsten (1990) decomposed the $C^{18}O$ emission from M17 SW into 179 elliptical, Gaussian clumps of sizes ranging from 4″ to 60″, FWHM linewidths from 0.5 to 3 km s^{-1}, and masses from 6 to 10^3 $M_\odot$. In principle, this clump model provides a complete picture for M17 SW; the model was used by Stutzki & Güsten to derive a clump mass spectrum for comparison to stellar initial mass functions. It is important to test this picture by trying to extend it to include emission in other lines.

In this section, we will see if the clumps inferred by Stutzki & Güsten can explain the observed CS emission. One requirement for the comparison of the clump model with our observations is that the clump parameters derived by Stutzki & Güsten must be consistent with those derived from the CS excitation analysis. The most striking differences between the clump parameters of Stutzki & Güsten and those derived from CS data are in the volume densities. Stutzki & Güsten (1990)

estimated the density of their clumps by dividing the column densities by sizes. In contrast to our virtually uniform density ($n = 5 \times 10^5$), Stutzki & Güsten obtained a rather large range of densities (10^4–10^7 cm^{-3}), with a mean of $10^{5.2}$ cm^{-3}. The most prominent clumps, which dominate the cloud morphology and the $C^{18}O$ line intensities, generally have densities $\sim 10^5$ cm^{-3}. The clumps with densities above $10^{5.2}$ cm^{-3} are mostly clumps with very small, and thus uncertain, sizes, which contribute little to the $C^{18}O$ emission. The only exceptions are the clumps located near the northern condensation, where clump densities are about $10^{5.4}$ cm^{-3}.

5.1. *Synthesis of Maps*

Using the properties of the clumps listed by Stutzki & Güsten, we synthesized CS maps for comparison with our observations. We computed line intensities along typically 5000 lines of sight, smoothed the results to our resolution, and compared the synthetic maps with the observations. As a test of our map synthesis code, we first synthesized the $C^{18}O$ $J = 2 \rightarrow 1$ channel maps and the total integrated line intensity map and compared them to the observed maps in Stutzki & Güsten (1990). The synthesized $C^{18}O$ maps correspond well with the observations in both morphology and intensity.

We then simulated the CS observations by synthesizing the CS $J = 1 \rightarrow 0$, $2 \rightarrow 1$, and $7 \rightarrow 6$ velocity channel maps. As input, we needed densities and column densities for each clump. We used the same procedure adopted by Stutzki & Güsten (basically, dividing column densities by linear sizes) to get density. To get the CS column density for each clump, we assumed a constant $C^{18}O$ to CS abundance ratio for all clumps. The observed intensities of the CS transitions near the northern condensation constrain the $C^{18}O$ to CS abundance ratio to be about 40, which gives a CS/H_2 abundance of 4×10^{-9}, assuming a $C^{18}O/H_2$ abundance of 1.6×10^{-7}. The CS/H_2 abundance is similar to those derived for other sources (Menten et al. 1987; Walker et al. 1990; Zhou et al. 1993). We used the LVG code to compute a line intensity from each clump, based on its density and column density, and then added the emission from all clumps intersected along the line of sight. Shadowing of clumps was not considered.

Figure 15 shows an example of the synthesized CS channel maps (V_{LSR} = 20–21 km s^{-1}) for each transition. The maps match the observed CS $J = 1 \rightarrow 0$ and $J = 2 \rightarrow 1$ morphologies and intensities near the northern condensation and along the ridge, but the synthesized CS $J = 2 \rightarrow 1$ channel maps show more prominent emission than was observed toward the

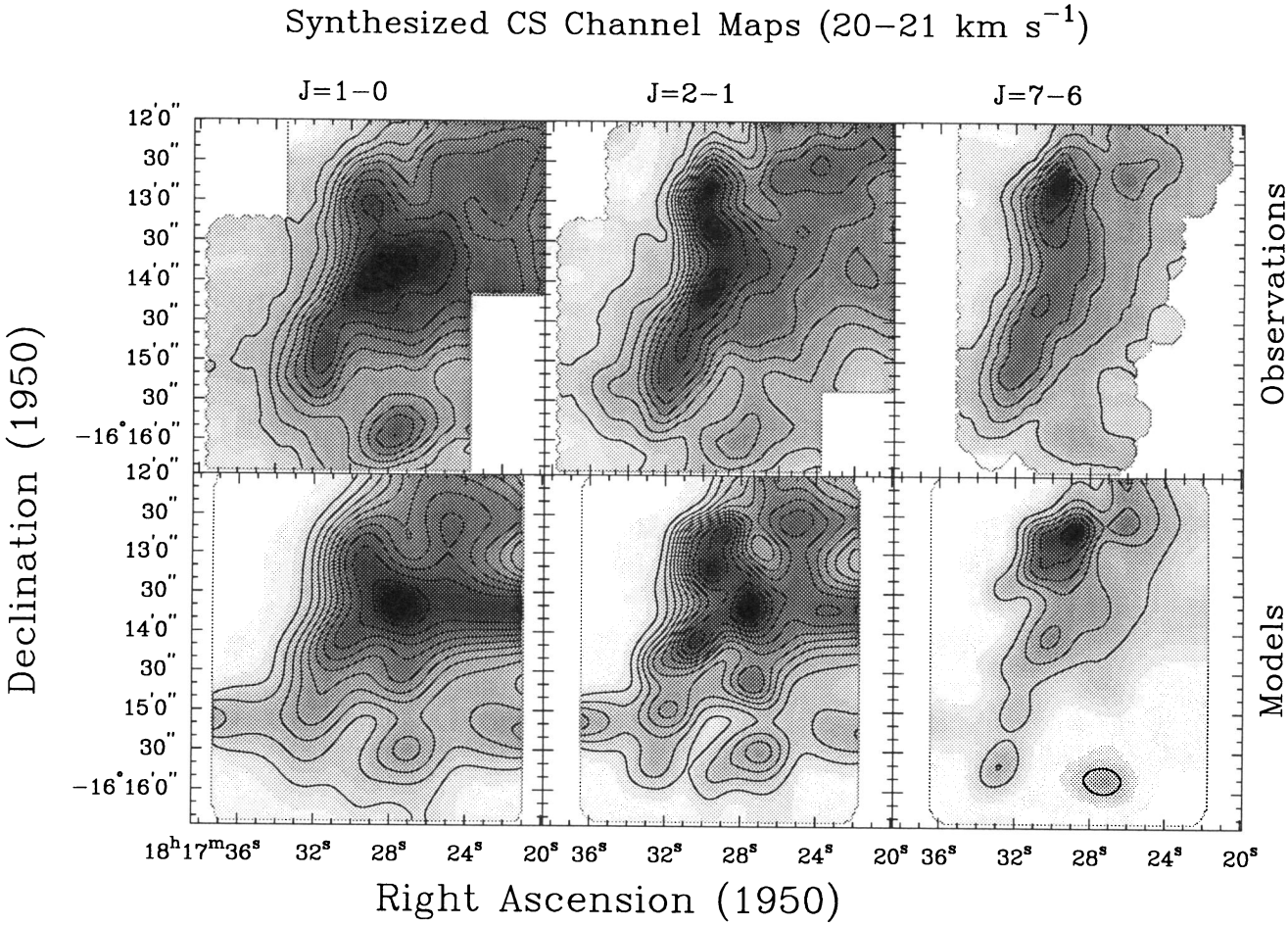

FIG. 15.—Comparison of the observed CS $1 \rightarrow 0$, $2 \rightarrow 1$, and $7 \rightarrow 6$ channel maps (V_{LSR} = 20–21 km s^{-1}) with the snthesized maps with the 179 clumps listed in Stutzki & Güsten (1990). A $C^{18}O$/CS abundance ratio of 40 is used to calculate N(CS). The lowest contours and the contour steps (1.0 K km s^{-1}) are the same for the synthesized maps and the observed maps. A linear gray scale is also shown in each panel to help distinguish minima from maxima. All synthesized maps are smoothed to the observed resolution.

central condensation and the isolated, southern condensation. In addition, the models predict stronger emission toward the west than is seen in the $J = 2 \rightarrow 1$ map (the region was not covered by the $J = 7 \rightarrow 6$ map). These discrepancies may result from both lower density and opacity effects, as noted in earlier sections.

The simulations of the $J = 7 \rightarrow 6$ line show a different pattern of disrepancies with the observations. No excess emission is predicted toward the southern condensation nor in the west. The synthesized CS $J = 7 \rightarrow 6$ map matches the observed intensities near the peaks of the northern and northwestern condensations, but has less intense emission along the ridge than the observations. This discrepancy is not surprising since only the Stutzki & Güsten clumps near the northern condensation and the northwestern condensation have densities within a factor of 2 of those derived from our CS analysis. The densities derived from the $C^{18}O$ for the other dominant clumps, most of which lie along the ridge, are too low ($\lesssim 10^5$ cm^{-3}) for these clumps to emit enough in the $J = 7 \rightarrow 6$ line to reproduce the observed emission. Increasing the CS abundance for the clumps along the ridge will increase both the CS $J = 7 \rightarrow 6$ emission and the CS $J = 2 \rightarrow 1$ emission along the ridge, leaving the ratio of the CS $J = 7 \rightarrow 6$ and $J = 2 \rightarrow 1$ lines almost unchanged. Therefore, the discrepancy between the synthesized maps and the observations along the ridge cannot be resolved by adjusting the CS abundance without adjusting the clump densities.

The discrepancies noted above indicate that clump densities determined using a column density tracer (e.g., $C^{18}O$) and a size does not reflect the local density characteristic of the gas emitting the CS lines. In particular, the $C^{18}O$ column density method seems to underestimate the density for the clumps along the ridge.

5.2. *Adjustments to the Model of Stutzki and Güsten*

To obtain better agreement with the observed CS maps, one could adjust both the volume density and CS abundance for each individual clump. However, the large number of free parameters would make such fine tuning meaningless. We instead considered the broad discrepancies noted above, not enough $J = 7 \rightarrow 6$ emission along the ridge and too much $J = 2 \rightarrow 1$ emission in the south and west. We considered two different ways to adjust the model. In both cases, we modified only the clump density, keeping the other clump parameters the same as in the previous simulation. In the first method, we scaled up all the individual clump densities derived from $C^{18}O$ by the same factor. In the second method, we assumed that all the clumps have some fixed density.

If we scale up the individual clump densities by a factor of 5, the synthesized maps agree best with the observations along the ridge. This scale factor, however, produced too much emission at the northern and northwestern condensations (Fig. 16). Therefore, for most of the clumps along the ridge, the densities derived from the $C^{18}O$ column densities and sizes are smaller

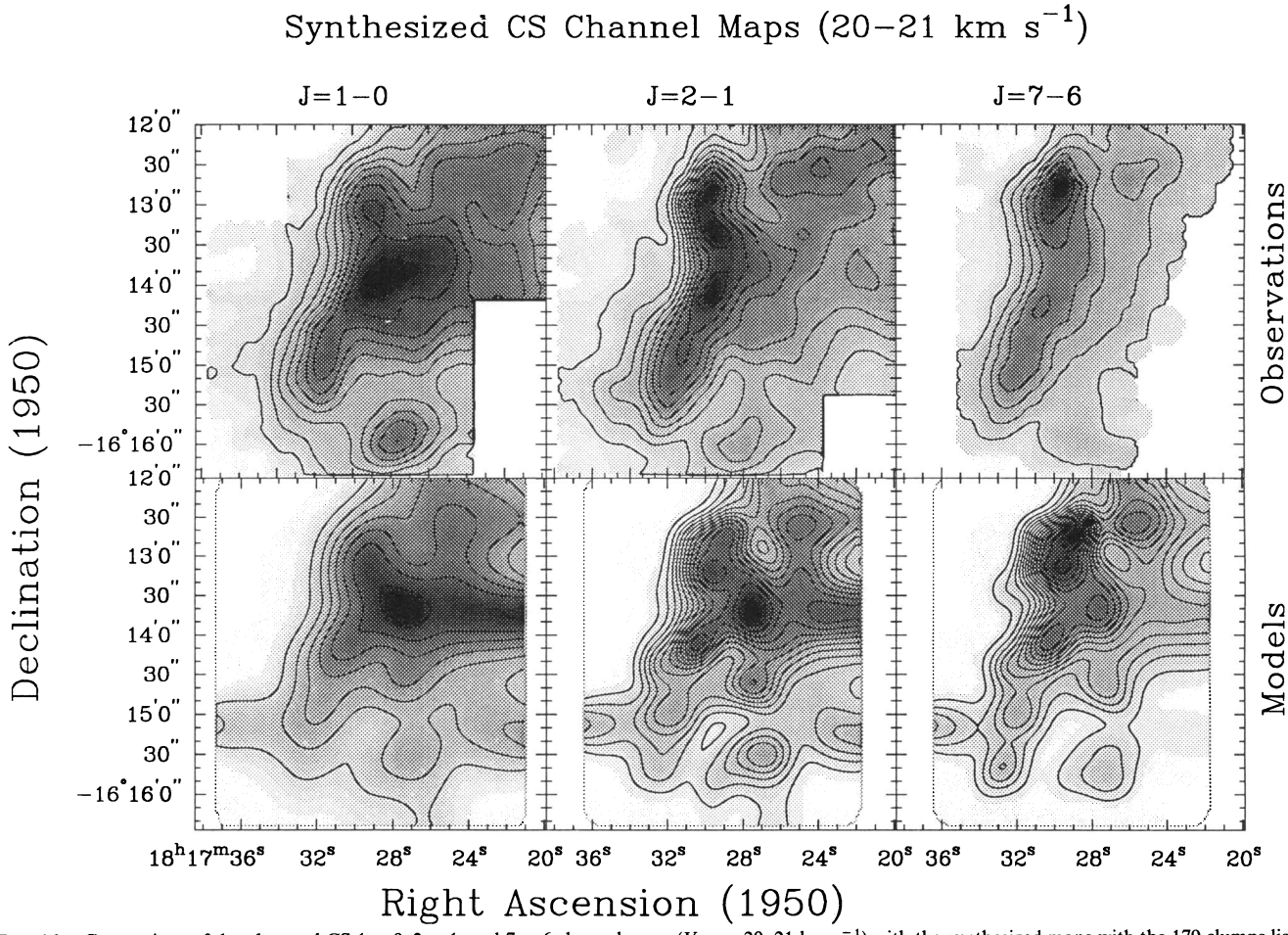

FIG. 16.—Comparison of the observed CS $1 \rightarrow 0$, $2 \rightarrow 1$, and $7 \rightarrow 6$ channel maps (V_{LSR} = 20–21 km s^{-1}) with the synthesized maps with the 179 clumps listed in Stutzki & Güsten (1990). The synthesized maps were calculated using the same model parameters as used in Fig. 15, except that the clump densities are scaled up by a factor of 5. The lowest contours and the contour steps (1.0 K km s^{-1}) are the same for the synthesized maps and the observed maps.

than the local gas density by a factor of ~5. The excess model emission in the south and west seen in Figure 16 is still present and is now a problem also for the CS $J = 7 \rightarrow 6$ line. This pattern indicates that simply scaling up the densities derived from $C^{18}O$ by a constant factor does not work over the whole map.

Among the models in which all clumps had the same density, a model with a density of 5×10^5 cm^{-3} reproduces the observations the best (Fig. 17). The synthesized maps now agree at the northern condensation and along the ridge, but the discrepancies in the south and west are still present. At velocities of 17–18 km s^{-1}, the synthesized maps for all lines predict a strong peak at the central condensation, which is actually observed only in the $J = 1 \rightarrow 0$ line. As discussed in § 3.3, the central condensation is weaker in the higher J lines partly because of opacity effects. Opacity may also be responsible for the weak emission from the southern condensation, since the $C^{34}S$ $J = 2 \rightarrow 1$ line has a peak there as well. A match to the ratio of $J = 1 \rightarrow 0$ and $2 \rightarrow 1$ lines toward this southern peak by lowering the density required a density too low (about 2×10^4 cm^{-3}) to be compatible with higher J lines.

Despite the differences between the synthesized maps and the observed CS maps, the agreement is reasonable; in particular, the degree of lumpiness is similar in both kinds of maps. In general, our simulations quantitatively support the assumption of Stutzki & Güsten (1990) that the $C^{18}O$ $J = 2 \rightarrow 1$ emission comes mainly from the dense clumps. As the $C^{18}O$ $J = 2 \rightarrow 1$ critical density is only about 10^4 cm^{-3}, any significant amount of lower density ($\lesssim 10^5$ cm^{-3}) gas between the dense clumps would contribute much more to the $C^{18}O$ $J = 2 \rightarrow 1$ emission than to the high-J CS emission. Therefore, the similar lumpiness of the synthesized maps and the observations implies that lower density gas does not make a significant contribution to the total column density and that the clump-interclump density contrast must be high.

The remaining puzzle is why the density required to explain the CS emission is usually higher than that derived from the $C^{18}O$ (e.g., by about a factor of 5 for the clumps along the ridge). The density difference may be caused by internal density structure in the clumps. If the clumps have a range of densities, the CS method of deriving densities will pick out the higher densities, while the $C^{18}O$ will give the average density. In general, either smooth density gradients or a continuation of high-contrast clumping to still smaller scales could account for the difference.

There are two arguments in favor of smooth density gradients over high-contrast clumping below the 0.15 scale of the observations of Stutzki & Güsten (1990). First a scale of 0.15–0.2 pc is the largest scale at which the smooth density gradient picture can work at all. In the previous CS analysis with 1′ (0.7

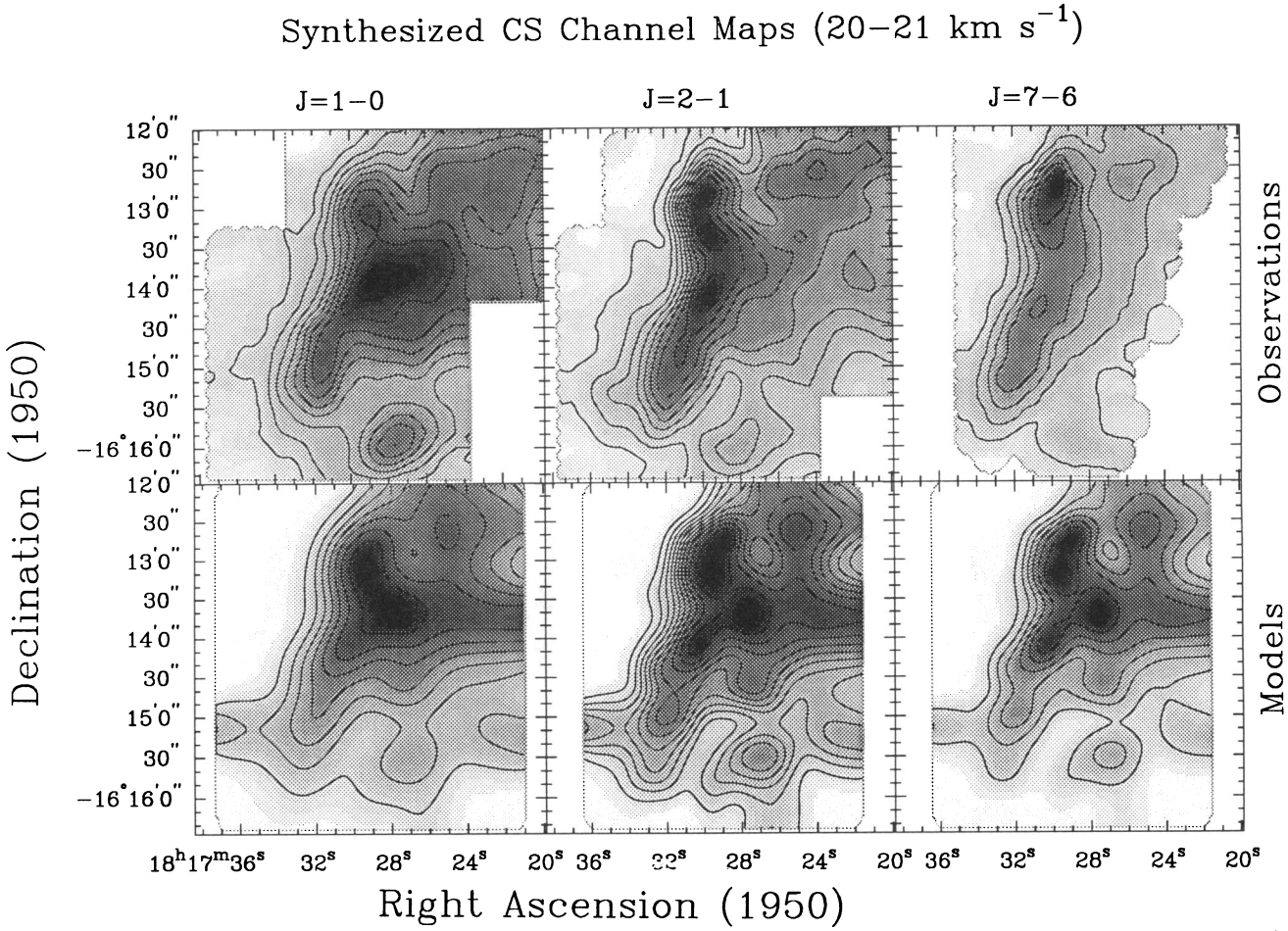

FIG. 17.—Comparison of the observed CS $1 \rightarrow 0$, $2 \rightarrow 1$, and $7 \rightarrow 6$ channel maps (V_{LSR} = 20–21 km s^{-1}) with the synthesized maps with the 179 clumps listed in Stutzki & Güsten (1990). The synthesized maps are calculated assuming a constant clump density ($n = 5 \times 10^5$ cm^{-3}) and a $C^{18}O$/CS abundance ratio of 40. The lowest contours and the contour steps (1.0 km s^{-1}) are the same for the synthesized maps and the observed maps.

pc) resolution, the derived densities were similar to those found in this work. The density derived from $C^{18}O$ analysis would have been smaller, however, since one would have been dividing by a larger size. Second, Stutzki & Güsten have argued that their clumps have sizes and masses similar to the Jeans lengths and masses for the physical parameters in the region. In this case, smooth gradients are expected as part of the collapse process (Larson 1969; Shu 1977). In the picture with continuation of high-contrast clumping, the dense cores would be much smaller than the Jeans length and would likely be transient structures.

None of these arguments for the Stutzki & Güsten clumps as physical entities, albeit with the addition of internal density structure, is totally convincing, but we tend to agree with those authors that at least the larger clumps that they deconvolved are physical entities. If the clumps have smooth density gradients, they may indeed be the precursors of individual stars, adding weight to considerations of the clump mass spectrum and its relevance to the initial mass function of stars.

6. SUMMARY

We summarize the main results of the paper as follows.

1. Extensive observations of M17 SW in CS and $C^{34}S$ lines were obtained with resolutions of 18″–36″ to study the structure of the dense gas. The velocity channel maps and the integrated intensity maps have complex morphology. Substructures with sizes of ~30″–120″ and linewidths of ~1–2 km s^{-1} exist throughout the cloud core.

2. The morphology of the CS maps is dominated by a prominent northern condensation west of the ionization front, an elongated emission feature at the H II/H_2 interface region, and a "central" condensation between these two features. There is general agreement in the overall morphology among maps of different CS and $C^{34}S$ lines, suggesting that all CS and $C^{34}S$ lines originate from the same dense gas. Modest morphological differences between these maps are caused by line opacity or excitation effects.

3. We carried out an excitation analysis with an LVG model, assuming uniform conditions along each line of sight, to derive the gas density and molecular column density along 252 lines of sight covering the entire 3′ × 4′ mapped region. The density map is mostly featureless, with an average density of about $10^{5.7}$ cm^{-3}, except for an area of more highly excited CS near the ionization front, where high temperature may artificially elevate the derived density. The derived CS column density map closely resembles the CS line temperature maps and reveals a ridge of enhanced column density along the H II/H_2 interface. The lack of a density enhancement along the ridge indicates that it is not the swept-up postshock layer envisioned in scenarios of sequential star formation (Elmegreen & Lada 1977).

4. The results of our excitation analysis show that peaks in the line temperature maps of a density tracer do not necessarily represent local density enhancements.

5. The simple, single-density LVG assumption was tested by including CS $J = 1 \rightarrow 0$ and $J = 5 \rightarrow 4$ lines in the analysis. For most of the positions where all four lines were observed, the single-density LVG model can adequately fit the observed line temperatures. The same analysis was also carried out using the $C^{34}S$ $J = 2 \rightarrow 1$, $3 \rightarrow 2$, and $7 \rightarrow 6$ lines. The derived gas densities from the $C^{34}S$ lines agree with those derived from the CS lines. Apparent isotopic ratios ($CS/C^{34}S$) range from 9 to 21, with an average ratio of about 13. Optical depth effects or unresolved structure in the emitting gas may cause the lower isotopic ratio, as compared to the terrestrial ratio of 22.

6. Along with other evidence, our excitation analysis suggests the existence of unresolved substructure in M17 SW. A simple clumpy cloud model in which the CS and $C^{34}S$ emission arises from numerous unresolved dense clumps is one type of substructure consistent with the major aspects of the observations and the results of the excitation analysis as well.

7. We carried out quantitative comparisons between the CS observations and the clump model put forward by Stutzki & Güsten (1990) based on the $C^{18}O$ $J = 2 \rightarrow 1$ data. Velocity channel maps of CS $J = 1 \rightarrow 0$, $2 \rightarrow 1$, and $7 \rightarrow 6$ transitions were synthesized using the parameters given in Stutzki & Güsten (1990) for 179 clumps in the region and compared with the observed maps. We found that the densities derived from $C^{18}O$ produced too little emission in the $J = 7 \rightarrow 6$ line to match the observations along the eastern edge, but a uniform gas density of 5×10^5 cm^{-3} and an abundance of CS of 4×10^{-9} is able to match the observed CS maps reasonably well. The need for a higher density to match the CS data can be reconciled with the $C^{18}O$ data if the clumps have internal density structure, for example, smooth density gradients or high-contrast clumping. While we cannot rule out smaller scale clumping, some arguments favor the idea that the clumps identified by Stutzki & Güsten (1990) are significant structures, much denser than the interclump medium, with internal density gradients, as might be expected from collapse processes.

We wish to thank J. Mangum and R. Plume for helping with part of the CSO observations. We are grateful to the staffs of the CSO and the NRO for their assistance and to J. Stutzki and R. Güsten for providing their $C^{34}S$ $J = 3 \rightarrow 2$ data. Y. W. thanks F. Bash for commenting on an early version of the manuscript. This work was supported by NSF grants AST 88-15801 and AST 90-17710, the Keck Foundation, and the Texas Advanced Research Program. D. J. acknowledges support from a David and Lucile Packard Foundation Fellowship.

REFERENCES

Chini, R., Elsässer, H., & Neckel, T. 1980, A&A, 91, 186
Crampton, D., Georgelin, Y. M., & Georgelin, Y. P. 1978, A&A, 66, 1
De Jong, T., Chu, Shih-I, & Dalgarno, A. 1975, ApJ, 199, 69
Downes, D., Wilson, T. L., Bieging, J., & Wink. J. 1980, A&AS, 40, 379
Elmegreen, B. G., & Lada, C. J. 1976, AJ, 81, 1089
———. 1977, ApJ, 214, 725
Elmegreen, B., Lada, C., & Dickinson, D. 1979, ApJ, 210, 415
Evans, N. J., II, Mundy, L. G., Davis, J. H., & Vanden Bout, P. 1987, ApJ, 312, 344
Felli, M., Churchwell, E., & Massi, M. 1984, A&A, 136, 53
Gatley, I., Becklin, E. E., Sellgren, K., & Werner, M. W. 1979, ApJ, 233, 575
Genzel, R., & Stutzki, J. 1989, ARA&A, 27, 11
Goldreich, P., & Kwan, J. 1974, ApJ, 189, 441
Greaves, J. S., White, G. J., & Williams, P. G. 1992, A&A, 257, 731
Green, S., & Chapman, S. 1978, ApJS, 37, 16
Güsten, R., & Fiebig, D. 1988, A&A, 204, 253
Harper, D. A., Low, F. J., Rieke, G. H., & Thronson, H. A. 1976, ApJ, 205, 136
Harris, A. I., Stutzki, J., Genzel, R., Lugten, J. B., Stacey, G. J., & Jaffe, D. T. 1987, ApJ, 322, L49,
Hobson, M. P. 1992, MNRAS, 256, 457
Jaffe, D. T., & Fazio, G. G. 1982, ApJ, 257, L77
Jaffe, D. T., Güsten, R., & Downes, D. 1981., ApJ, 250, 621

Kleinmann, E., & Wright, 1973, Ap. Lett, 13, 49
Kraus, J. D. 1986, Radio Astronomy (2d ed.; Powell, Ohio: Cygnus-Quasar Books)
Kutner, M. L., & Ulich, B. L. 1981, ApJ, 250, 341
Lada, C. J. 1976, ApJS, 32, 603
Lada, C. J., DePoy, D. L., Merrill, K. M., & Gatley, I. 1991, ApJ, 374, 533
Lada, E. A. 1992, ApJ, 393, L25
Larson, R. 1969, MNRAS, 145, 271
Liszt, H., & Leung, C. 1977, ApJ, 218, 396
Martin, H. M., Sanders, D. B., & Hills, R. E. 1984, MNRAS, 208, 35
Meixner, M., Haas, M., Tielens, A., Erickson, E., & Werner, M. 1992, ApJ, 390, 499
Menten, K. M., Serabyn, E., Güsten, R., & Wilson, T. L. 1987, A&A, 177, L57
Mezger, P. G., Chini, R., Kreysa, E., Wink, J. E., & Salter, C. J. 1988, A&A, 191, 44
Moore, T. J. T., Chandler, C. J., Gear, W. K., & Mountain, C. M. 1989, MNRAS, 237, 1P
Mundy, L., Snell, R. L., Evans, N. J., II., Goldsmith, P. F., & Bally, J. 1986, ApJ, 306, 670
———. 1987, ApJ, 318, 392
Myers, P. C. 1987, in Interstellar Processes, ed. D. J. Hollenbach & H. A. Thronson, Jr. (Dordrecht: Reidel), 72
Ogura, K., & Ishida, K. 1976, PASJ, 28, 35
Penzias, A., & Burrus, C. 1973, ARA&A, 11, 51
Rainey, R., White, G. J., Gatley, I., Hayashi, S. S., Kaifu, N., Griffin, M. J., & Monteiro, T. S. 1987, A&A, 171, 252
Schulz, A., Güsten, R., Zylka, R., & Serabyn, E. 1991, A&A, 246, 570
Schulz, A., & Krügel, E. 1987, A&A, 171, 297
Scoville, N. Z., & Solomon, P. M. 1974, ApJ, 187, L67
Shu, F. 1977, ApJ, 214, 488
Snell, R. L. 1981, ApJS, 45, 121
Snell, R. L., Erickson, N. R., Goldsmith, P. F., Ulich, B. L., Lada, C. J., Martin, R. N., & Schulz, A. 1986, ApJ, 304, 780
Snell, R. L., Mundy, L. G., Goldsmith, P. F., Evans, N. J., II., & Erickson, N. R. 1984, ApJ, 276, 625
Stutzki, J., & Güsten, R. 1990, ApJ, 356, 513
Stutzki, J., Stacey, G. J., Genzel, R., Harris, A. I., Jaffe, D. T., & Lugten, J. B. 1988, ApJ, 322, 379
Thronson, H., & Lada, C. 1983, ApJ, 269, 175
Walker, C. K., Carlstrom,, J. E. Bieging, J. H., Lada, C. J., & Young, E. T. 1990, ApJ, 364, 173
Welch, W. J., Dreher, J. W., Jackson, J. M., Terebey, S., & Vogel, S. N. 1987, Science, 238, 1550
White, R. E. 1976, ApJ, 211, 744
Wilson, T. L., Fazio, G. G., Jaffe, D., Kleinmann, D., Wright, E. L., & Low, F. J. 1979, A&A, 76, 86
Wilson, T. L., & Mauersberger, R. 1990, A&A, 239, 305
Zhou, S., Evans, N. J., II., Kömpe, C., & Walmsley, C. M. 1993, ApJ, 404, 232
Zuckerman, B., & Evans, N. J., II. 1974, ApJ, 192, L149